INL/RPT-23-72727

Fluoride-Cooled High-Temperature Pebble-Bed Reactor Reference Plant Model

May 2023

Javier Ortensi[1], Cole M. Mueller[2], Stefano Terlizzi[1], Guillaume Giudicelli[3], and Sebastian Schunert[1]

[1]*Reactor Physics Methods and Analysis*
[2]*Former Thermal Fluid Systems Methods and Analysis*
[3]*Computational Frameworks*

INL is a U.S. Department of Energy National Laboratory
operated by Battelle Energy Alliance, LLC

INL/RPT-23-72727

Fluoride-Cooled High-Temperature Pebble-Bed Reactor Reference Plant Model

Javier Ortensi[1], Cole M. Mueller[2], Stefano Terlizzi[1], Guillaume Giudicelli[3], and Sebastian Schunert[1]

[1]**Reactor Physics Methods and Analysis**
[2]**Former Thermal Fluid Systems Methods and Analysis**
[3]**Computational Frameworks**

May 2023

Idaho National Laboratory
Nuclear Science and Technology
Idaho Falls, Idaho 83415

http://www.inl.gov

Prepared for the
Office of Nuclear Regulatory Research
U. S. Nuclear Regulatory Commission
Washington, D. C. 20555
Task Order No.: 31310019F0015

Page intentionally left blank

SUMMARY

In this report we present work performed in Fiscal Year 2022 that demonstrates the modeling and simulation of a fully coupled neutronics thermal hydraulics reference plant model for a fluoride-cooled high-temperature pebble-bed reactor. The multiphysics model is developed on the Nuclear Regulatory Commission's Comprehensive Reactor Analysis Bundle (BlueCRAB) available on the Idaho National Laboratory's high-performance computer, which natively and seamlessly couples the Griffin and Pronghorn Object-Oriented Simulation Environment based applications. Griffin provides reactor physics capabilities, including depletion to the equilibrium core, k-eigenvalue, adjoint, and transient. The unique direct equilibrium core capability in Griffin is based on a streamline methodology to spatially deplete the pebbles into burnup groups. Pronghorn solves the porous medium equations for the fluid regions and conduction in the solid regions and incorporates a fluidic diode model to simulate the transition from forced to natural convection during accident scenarios. MOOSE modules solves thermal conduction problems for the pebbles and tristructural isotropic particles in the pebble-bed core, thus providing the fuel and moderator spatial fields for each pebble burnup group. The neutronics feedback relies primarily on fuel, moderator, and reflector temperatures as as well as the FLiBe salt density. Here, we present results for the uncoupled equilibrium core and perform comparisons to equivalent Monte Carlo models. The power distributions and kinetic parameters obtained with Griffin are consistent with those computed with Serpent. We demonstrate a noticeable improvement with the use of discrete ordinates method (SN) transport over diffusion with the flux-limited in-scatter approximation of the transport cross section. The coupled steady-state equilibrium core provides the initial condition for two time-dependent problems: a control rod withdrawal event and an unprotected loss of flow event. In both cases, the reactor design is self-stabilizing and the solutions are consistent with the expected physics. Although this model is prototypical regarding BlueCRAB's capabilities, its results

are consistent with published work by Kairos Power and other research entities. Significant improvements to the model are planned in future work.

ACKNOWLEDGEMENTS

This research made use of the resources provided by the Nuclear Energy Advanced Modeling and Simulation (NEAMS) program managed by the Department of Energy Office of Nuclear Energy.

This research made use of the resources of the High Performance Computing Center at Idaho National Laboratory, which is supported by the Office of Nuclear Energy of the U.S. Department of Energy and the Nuclear Science User Facilities under Contract No. DE-AC07-05ID14517.

Description of the various author roles:

- Javier Ortensi—conceptual development, cross sections, neutronics model development, analysis
- Cole M. Mueller—thermal fluids model development, coupled model analysis
- Stefano Terlizzi—neutronics control rod model development, control rod model
- Sebastian Schunert—code development (NEAMS), thermal fluids model development
- Guillaume Giudicelli—code development (NEAMS), thermal fluids model development

Special thanks to Paolo Balestra for his review of this document and all of his contributions to this work through our, sometimes prolonged, discussions.

This work would not have been possible without the contributions from the Idaho National Laboratory Griffin development team: Yaqi Wang, Sebastian Schunert, Zach Prince, Vincent Labouré, Josh Hanophy, and Olin Calvin.

We are grateful to all Multiphysics Object-Oriented Simulation Environment developers that supported this work, including Alexander Lindsay, Logan Harbour, Fande Kong, Guillaume Giudicelli, and Derek Gaston.

Finally, we would like to thank Liam Carlson for computing the spatial distribution of the pebble packing fraction.

Page intentionally left blank

CONTENTS

FIGURES

TABLES

ACRONYMS

AGR Advanced Gas Reactor development and qualification program

DB Dittus-Boelter

EFPD effective full power days

gFHR generic fluoride-cooled high-temperature reactor

KPACS Kairos Power Advanced Core Simulator

MOL middle of life

PBR Pebble-Bed Reactor

PHSS pebble handling and storage system

SN discrete ordinates method

SPH superhomogenization

Page intentionally left blank

1. INTRODUCTION

The design of the generic fluoride-cooled high-temperature reactor (gFHR) is based on published material by Kairos Power [1]. The geometry is shown in Figure 1, including the active core, reflector, core barrel, salt downcomer, and reactor vessel regions.

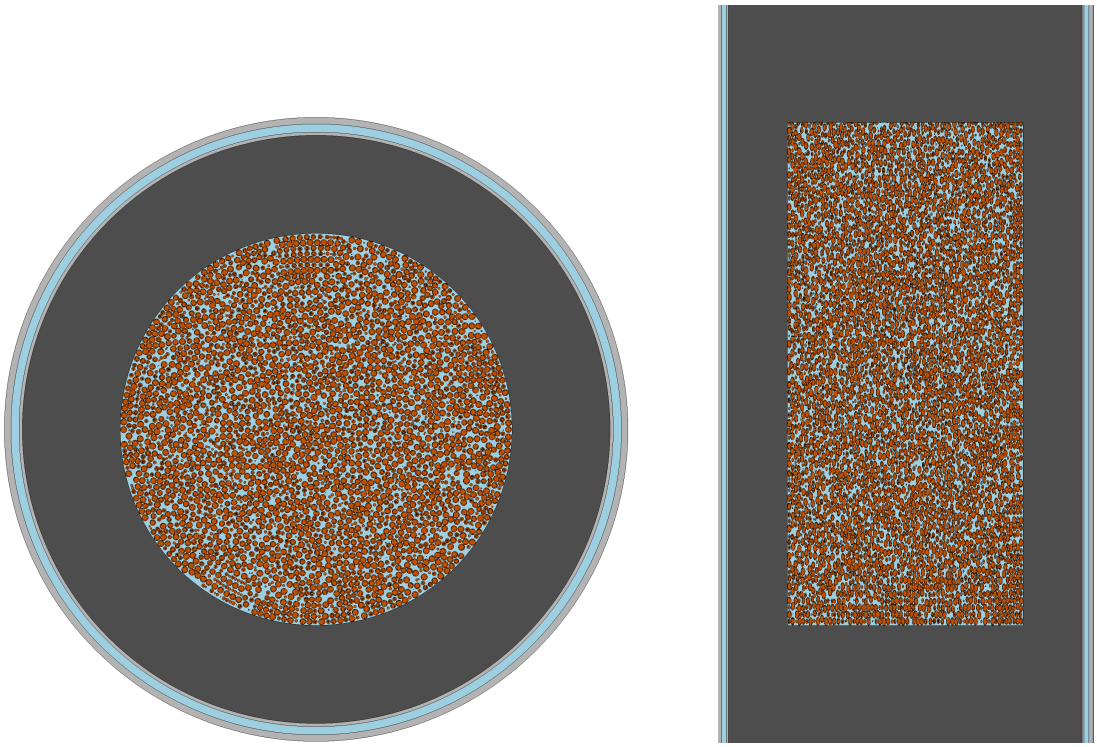

(a) Radial view (b) Axial view

Figure 1: gFHR conceptual design.

The main characteristics of the core design are included in Table 1. This design relies on a multipass strategy in which the pebbles are discharged at the top of the active core and then reintroduced uniformly at the bottom of the core. The pebbles are buoyant and float toward the top of the core. The pebbles undergo an average of eight passes before they are discharged. The recirculation, evaluation, and disposal tasks are performed by the pebble handling and storage system (PHSS). During the evaluation task, the PHSS determines if the pebble has achieved the desired design burnup, at which point it is either discharged or recirculated back to the bottom of the core. Note that the average residence time in the original journal article [1] was approximated between 490 and 550 effective full power days (EFPD).

Table 1: gFHR reactor specifications [1].

Parameter	Value
Core power [MWth]	280
Core inlet temperature [K]	823.15
Core outlet pressure [Pa]	2e5
Pebble bed radius [m]	1.2
Pebble bed height [m]	3.0947
Number of pebbles	250,190
Pebble types	One pebble type (3.4g IHM)
Pebble packing fraction (average)	0.6
Average number of passes	8
Average pebble residence time [days]	522
Reflector outer radius [m]	1.8
Barrel outer radius [m]	1.82
Downcomer outer radius [m]	1.87
Vessel outer radius [m]	1.91
Reflector graphite density [kg/m^3]	1,740.0
SS 316H density (barrel and vessel) [kg/m^3]	8,000.0

This benchmark uses a single pebble design or type. The pebble specifications are shown in Table 2. The pebble includes a spherical lower density center graphite core for buoyancy, followed by a spherical shell that contains the TRISO particles and an outer spherical graphite shell.

Table 2: Pebble specifications [1].

Parameter	Value
Pebble core radius [cm]	1.380
Fuel layer radius [cm]	1.8
Shell layer radius [cm]	2.0
Number of particles per pebble	11,660
Pebble core graphite density [kg/m^3]	1,410.0
Fuel layer matrix density [kg/m^3]	1,740.0
Shell layer graphite density [kg/m^3]	1,740.0

The TRISO design specifications are included in Table 3. These specifications are based on the oxycarbide fuel testing from the Advanced Gas Reactor development and qualification program (AGR) AGR-2 irradiation campaign [2] with the carbon content set to the upper limit of the AGR testing envelope.

Table 3: TRISO specifications [1].

Parameter	Value
Fuel kernel radius [cm]	0.0212
Buffer outer radius [cm]	0.03125
IPyC outer radius [cm]	0.03525
SiC outer radius [cm]	0.03875
OPyC outer radius [cm]	0.04275
Fuel type	$UC_{0.5}O_{1.5}$
Fuel enrichment	19.55%
Fuel kernel density [kg/m^3]	10,500.0
Buffer graphite density [kg/m^3]	1,050.0
IPyC, OPyC graphite density [kg/m^3]	1,900.0
SiC density [kg/m^3]	3,180.0
Matrix graphite density [kg/m^3]	1,740.0

2. ANALYSIS METHODOLOGY

The majority of the applications deployed to perform this analysis are developed under the Multiphysics Object-Oriented Simulation Environment (MOOSE) framework [3]. Section 2.1 introduces the reactor physics methods and Griffin reactor multiphysics application. The thermal fluids solver Pronghorn is described in Section 2.2.

2.1 Reactor Physics Methods

Griffin is a reactor multiphysics application built on MOOSE and based on the technology developed for Rattlesnake [4], Mammoth [5], and PROTEUS [6]. Griffin provides neutron transport, depletion, core performance, decay heat, and cross-section calculation capabilities for non-light-water advanced reactor technologies. In this work, we use both Griffin's diffusion and the discrete ordinates method (SN) approximation to solve the linearized Boltzmann transport equation with the multigroup approximation in the energy domain. In order to perform neutronics and depletion calculations with Griffin, multigroup cross sections need to be provided as a function of reactor state parameters, such as temperature and burnup. Alas, the cross-section preparation capability for Pebble-Bed Reactor (PBR)s in Griffin is not currently available, but should be ready for testing at the end of September 2023. In lieu of Griffin cross sections, we rely on DRAGON [7, 8] to prepare microscopic cross sections in this work. Serpent, a three dimensional (3D) continuous-energy Monte Carlo reactor physics code developed at the VTT Technical Research Centre of Finland [9], provides detailed reference calculations without energy, angular, or spatial discretization approximations.

2.1.1 Cross-Section Preparation

There are important limitations to the approach herein since the neutron leakage in this reactor significantly affects the local spectrum [10]. Nevertheless, this data set serves as an initial set to perform preliminary calculations until more sophisticated methods are available in Griffin. The neutron cross sections used with DRAGON in this work are based on the ENDF/B-VII.r1 SHEM 281 library.

The subgroup self-shielding method and SN spatial flux solution in DRAGON are deployed

to prepare the microscopic cross sections. The following 1D spherical calculations are performed:

1. Single pebble depletion at a constant power of 328.55W/gU to compute a middle of life (MOL) flux level
2. Single pebble depletion at a constant flux of $4.6 \times 10^{14}\,\mathrm{n/cm^2/s}$ (obtained from Step 1)
3. Single pebble depletion in a pebble ensemble with MOL ($\sim$264 days) compositions at a constant flux of $4.6 \times 10^{14}\,\mathrm{n/cm^2/s}$
4. Pebble branch cases with isotopics from Step 3 in a MOL pebble ensemble
5. Pebble branch cases with isotopics from Step 3 in a MOL pebble ensemble near a reflector.

The microscopic cross sections are condensed from 281 to four energy groups and homogenized over the pebble. The four energy group structure is show in Table 4.

Table 4: Neutron energy group boundaries for the four group structure.

Neutron Energy [eV]
1.96403000E+07
1.95007703E+05
1.75647602E+01
2.33006096E+00
1.10002700E-04

The isotope transport cross sections are based on a "flux-limited" approximation [11] or in-scatter approximation with scalar flux as a weighting function [12]:

$$\sigma_{tr}^{g} = \sigma_{t}^{g} - \sum_{g'=1}^{G} \sigma_{s_1}^{g'->g} \frac{\phi^{g'}}{\phi^{g}} \tag{1}$$

The main contributors to the reactor feedback mechanism in the gFHR are attributed to changes in:

- Fuel temperature — the fuel kernel temperature
- Moderator temperature — temperature of all of the materials in the pebble with the exception of the fuel kernel
- Reflector temperature — graphite reflector temperature

- Coolant density — FLiBe density.

The tabulated values for the active core region cross sections are shown in Table 5 and are intended for supporting a transient analysis.

Table 5: gFHR model microscopic cross-section parameters for the active core region.

Parameter	Value
Number of isotopes	297
Burnup tabulation [days]	0.0, 264, 650
Burnup tabulation [J/m^3]	0.00, 8.494×10^{14}, 1.759×10^{15}
Fuel temperature tabulation [K]	600.0, 859.0, 959.0, 1059.0, 1200.0, 1600.0
Moderator temperature tabulation [K]	600.0, 800.0, 900.0, 1000.0, 1200.0
Coolant density tabulation [kg/m^3]	1,925.0, 1,973.8, 2,022.6, 2,120.2

Macroscopic cross sections are prepared for the reflector, steel structures, and downcomer with a 1D cylindrical solution of the core with the DRAGON SN solver in 281 energy groups and homogenized to four broad energy groups. The spectrum is generated from a fuel mix with MOL compositions. The tabulation points are shown in Table 6.

Table 6: gFHR model macroscopic cross-section parameters.

Parameter	Value
Reflector temperature tabulation [K]	600.0, 900.0, 1200.0
SS 316H temperature tabulation [K]	600.0, 900.0, 1200.0
Downcomer coolant density tabulation [kg/m^3]	1,925.0, 1,973.8, 2,120.2

2.1.2 Equilibrium Core Calculation

The equilibrium core is attained via the streamline depletion method available in Griffin. In this depletion approach, the 2D and 3D core flux solution is mapped to a set of 1D axial streamlines. A set of 1D steady-state advection-transmutation equations for all isotopes are solved in each streamline to obtain the equilibrium core solution [13]. Griffin assumes that the pebble loading and unloading rates are identical.

The fraction of volume occupied by pebbles (i.e., packing fraction) on streamline k at position s is denoted by $n_k(s)$.

$$n_k(s) = \text{Packing fraction} = \frac{\text{Volume occupied by pebbles}}{\text{Total volume}} \tag{2}$$

The definition on the right-hand side of Equation 2 is: at location s along streamline k, a representative volume centered at s is selected that contains a sufficient number of pebbles. The total extent of this representative volume is the denominator of Equation 2, while the portion occupied by the pebbles is the numerator. Both the numerator and denominator on the right-hand side of Equation 2 depend on s and index k, but we omit these details for brevity. We treat $n_k(s)$ as a continuous function, implying that $n_k(s)$ can be meaningfully evaluated at a given point, even though defining $n_k(s)$ requires a representative volume of finite size.

We denote the packing fraction occupied by a pebble of type c, as identified by its initial composition on streamline k, by $n_{c,k}$. The packing fraction $n_{c,k}(s,\tau)$ depends on the distance (s) measured along the streamline from the core inlet and on burnup (τ):

$$n_{c,k}(s,\tau)d\tau = \frac{\left[\begin{array}{l}\text{Volume occupied by a pebble of type } c \\ \text{identified by initial composition on streamline } k \\ \text{with burnup between } \tau \text{ and } \tau + d\tau\end{array}\right]}{\text{Total volume}} \tag{3}$$

The relationship between $n_{c,k}(s,\tau)$ and $n_k(s)$ is:

$$n_k(s) = \sum_{c=1}^{C} \int_0^\infty n_{c,k}(s,\tau)d\tau \tag{4}$$

As a short-hand, we will refer to pebble type c (identified by its initial composition) as simply "type c."

The balance equation for $n_{c,k}(s,\tau)$ along the streamline is:

$$\begin{aligned}&\frac{\partial\left(u_k(s)A_k(s)n_{c,k}(s,\tau)\right)}{\partial s} \\ &+ A_k(s)\frac{\partial\left(p_c(\vec{r}_k(s),\tau)n_{c,k}(s,\tau)\right)}{\partial\tau} = 0\end{aligned} \tag{5}$$

where $p_c(\vec{r}_k(s),\tau)$ is the power density that a pebble of type c with a burnup between τ and $\tau + d\tau$ experiences.

The fraction of volume occupied by pebbles of type c with burnups falling into group l is given by:

$$n_{c,k,l}(s) = \int_{\tau_l}^{\tau_{l+1}} n_{c,k}(s,\tau)d\tau \tag{6}$$

Integrating Equation 5 over τ within $[\tau_l, \tau_{l+1}]$ gives:

$$\begin{aligned} &\frac{\partial\left(u_k A_k n_{c,k,l}(s)\right)}{\partial s} \\ &+ A_k\left[p_c(\tau_{l+1})n_{c,k}(\tau_{l+1}) - p_c(\tau_l)n_{c,k}(\tau_l)\right] = 0 \end{aligned} \tag{7}$$

where obvious arguments are omitted for convenient notation. We approximate $p_c(\tau_l)n_{c,k}(s,\tau_l)$ using upwinding in the direction of increasing burnup:

$$p_c(\tau_l)n_{c,k}(\tau_l) \approx \begin{cases} 0 & \text{if } l = 1 \\ 0 & \text{if } l = L+1 \\ \frac{\overline{p}_{c,l-1}n_{c,k,l-1}}{\Delta\tau_{l-1}} & \text{else} \end{cases} \tag{8}$$

where $\Delta\tau_l = \tau_{l+1} - \tau_l$ and the average power is defined by:

$$\overline{p}_{c,l}(\vec{r}_k(s)) = \frac{1}{\Delta\tau_l}\int_{\tau_l}^{\tau_{l+1}} p_c(\vec{r}_k(s),\tau)d\tau \tag{9}$$

This result leads to the semidiscrete form of Equation 7:

$$\frac{\partial\left(u_k A_k n_{c,k,l}\right)}{\partial s} + A_k\left[\frac{\overline{p}_{c,l}n_{c,k,l}}{\Delta\tau_l} - \frac{\overline{p}_{c,l-1}n_{c,k,l-1}}{\Delta\tau_{l-1}}\right] = 0 \tag{10}$$

This equation couples the population of pebbles in burnup group l and at location s to the neighboring burnup group $l-1$ and neighboring locations. When discretizing the derivative with respect to τ, we used a constant approximation of power over each burnup group (i.e., $p_c(\vec{r}_k(s),\tau_l) \approx \overline{p}_{c,l}(\vec{r}_k(s))$).

2.2 Thermal Fluids Methods

This section discusses the various methods used for solving the thermal fluid fields. We deploy the Pronghorn porous media formulation of the Navier-Stokes equations with a weakly-compressible fluid spatially discretized with the finite volume method [14, 15]. This is a low mach formulation that results in a change to the fluid energy equation called "Weakly Compressible"

within the MOOSE framework. The momentum equation is altered from the traditional Navier-Stokes relationship by replacing the viscous diffusion term with porous friction term comprised of Darcy and Forchheimer correlated friction relationships. The mass conservation equation is a standard porosity weighted equation. These three can be seen in Equation 11 with them listed from top to bottom as Mass, Momentum, and Energy Conservation, respectively. This is then solved using a finite volume discretization scheme using a Rhie-Chow interpolation.

$$\begin{aligned} \gamma\frac{\partial\rho}{\partial t} + \nabla\cdot(\rho\vec{v}) &= 0 \\ \frac{\partial\rho\vec{v}}{\partial t} + \nabla\cdot(\gamma^{-1}\rho\vec{v}\otimes\vec{v}) &= -\gamma\nabla p + \gamma\rho\vec{g} - W\rho\vec{v} \\ \gamma\frac{\partial\rho e}{\partial t} + \nabla\cdot(\rho h\vec{v}) - \nabla\cdot(\kappa_f\nabla T) + \alpha(T-T_s) &= 0 \end{aligned} \tag{11}$$

In a porous media problem, there are multiple ways equations can be written. The MOOSE framework assumes the fluid and solid energy conservation equations are handled distinctly and coupled through a heat transfer coefficient. As a result, the solid temperature field must be solved to fully define the system. This solution is based off the solid energy conservation equation seen in Equation 12, which includes internal heat generation so that the heat produced within the fuel of the pebbles within our core can be accurately captured. The other three terms, from left to right, are the transient energy accumulation, the thermal diffusion, and the fluid solid energy coupling. These are implemented as kernels within the system of equations because the module within MOOSE only handles the fluid side of the equations.

$$(1-\gamma)\rho_s c_{p,s}\frac{\partial T_s}{\partial t} - \nabla\cdot(k_s\nabla T_s) - \alpha(T-T_s) = \dot{q}''' \tag{12}$$

Appropriately modeling the homogenized pebble bed requires several closures to obtain accurate effective bed properties. For the fluid momentum equations, this was captured in the porous media relations specifically relating to Darcy and Forchheimer coefficients to capture the large additional resistances caused by the constrained tortuous flows. Similarly, the thermal properties need to be properly resolved in a homogenized manner to obtain accurate temperature distributions. Within the fluid region, only one single effective property is needed, κ_f, which is the effective conductivity of the fluid in the porous media. This effective conductivity of the fluid also includes convection terms that incorporate the mixing (convective phenomena) due

to the tortuous path that the fluid experiences in the pebble-bed. For the solid medium there is also one single effective property but it is more complicated as a pebble-bed reactor will have more interaction modes from pebble to pebble across flow channels than the fluid does across pebbles. These interaction modes are radiation, solid conduction through the pebbles, and fluid conduction. For the radiation component, we use the Breitbach and Barthels model. This may not be appropriate for molten-salt reactors as the radiative connection between pebbles is likely different than in gas-cooled reactors where this correlation was developed. It is still included as placeholder for a salt-cooled reactor correlation in the future. The sphere-to-sphere conduction is handled with the Chan and Tien model. Then, finally, the fluid conduction component is handled with the Zehner, Bauer, and Schlunder (ZBS) model. These four effective properties are shown in Equation 13, and further details are in the Pronghorn user manual and its referenced sources [16].

$$\begin{aligned}
\kappa_f &= \epsilon k_f + C_0 Pe k_f \\
\kappa_{\text{radiation}} &= \left[\left(1 - \sqrt{1-\epsilon}\right) \epsilon + \frac{\sqrt{1-\epsilon}}{2/\epsilon_{r,s} - 1} \frac{B+1}{B} \frac{1}{1 + \frac{1}{(2/\epsilon_{r,s}-1)\Lambda}} \right] 4\sigma d_p \bar{T}^3 \\
\kappa_{\text{solid conduction}} &= \frac{1}{2 \cdot 0.53} \frac{N_A}{N_L} \left(\frac{d_c}{d_p} \right) d_p \lambda k_f \\
\kappa_{\text{fluid conduction}} &= (1 - \sqrt{1-\epsilon}) k_f + \sqrt{1-\epsilon} K_{SF} k_f
\end{aligned} \tag{13}$$

There is a final coupling parameter between the solid and fluid energy equations, and this is a type of heat transfer coefficient. Normally, a heat transfer coefficient would describe the relationship between the bulk fluid temperature, the surface temperature, and the heat flux locally at that surface. However, in this system this is not the case. There is not really an explicit surface for the heat to transfer through in our homogenized problem. Instead, a surface density is determined from the porosity of the medium. This goes back to the definition of the solid energy equation. The solid energy equation is solving for an effective solid temperature based on the correlation measurements for the heat transfer coefficient. The heat transfer coefficient then acts as a volumetric source coefficient where the local fluid energy source, and subsequently solid energy sink, is proportional to the difference between the local solid and fluid temperatures. However, these correlations still use similar Nusselt formulations to obtain the heat transfer coefficient. This

model used a Petrovic heat transfer coefficient formulation as seen in Equation 14. For more information on these models, please refer to the Pronghorn manual and its referenced sources [16].

$$Nu = 0.357 \frac{Pr^{1/3}}{\epsilon} Re^{0.641} \tag{14}$$

2.2.1 Fluidic Diode

In order to constrain the coolant flow in a single direction in the bypass channel, a volumetric friction flow diode was added to Pronghorn. The volumetric friction slows down the flow in both directions when turned on with a Boolean parameter specified in the input file. This was preferred over having the friction term in only a single flow direction for a few reasons. Even though a flow diode should always let flow pass in one direction, the current use case has a strong difference between the two sides of the diode, so flow would not go in the passing direction of the diode.

Having a friction term that turns on and off based on the current fluid velocity has been problematic for convergence. Since the flow is very small with high friction, the velocity may flip during the numerical solve, turning off the friction in the region. A smooth friction transition between allowed and blocked flow would be required. Having the diode be partially blocked depending on the local velocity in a volume is also not desirable.

A Boolean parameter, which can be dynamically set using the MOOSE control system, does not fluctuate during each time step solve and can still let the flow through at any arbitrary time and under any arbitrary condition. It improves the diode stability, while not really limiting its flexibility.

Testing the diode through flow rate computations The friction flow diode is demonstrated in the system pictured in Figure 2. The system inlet is on the top right side, with the outlet on the top left side. There are two flow paths connecting both sides, one at the top and one at the bottom of the system, and the top one includes the friction diode. Without an active diode, close to 80% of the flow would flow through the top channel as it is shorter and incurs much less friction from the porous medium.

We test the effectiveness of the friction diode by increasing the additional linear friction factor

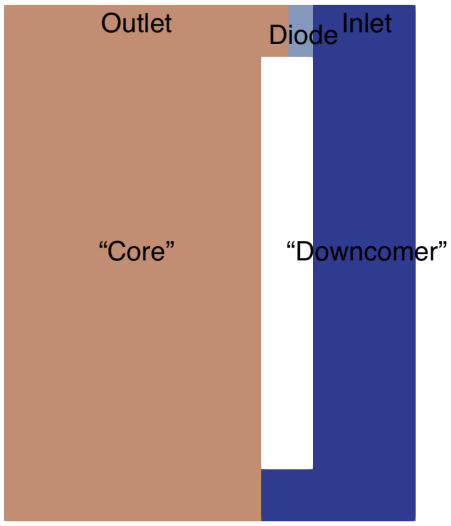

Figure 2: Test system for the diode.

and report the results in Table 7. We see a rather large additional friction factor is required to reduce the flow, but its effectiveness at reducing the flow rate is proven. As the flow is reduced through the diode channel, the pressure drop increases as the flow is pushed through a longer flow path through the bottom channel.

Table 7

Additional diode linear friction	Inlet-outlet pressure drop (kPa)	Percent flow through diode (%)
0 (open diode)	86.5	49.4
10	90.9	48.1
1e2	115.9	41.2
1e3	210.9	18.9
1e4	294.3	3.1
1e5	310.3	0.33

Stabilization and friction correction The discontinuity in the friction coefficients, and therefore in the friction forces, between the region neighboring the diode and the diode itself causes numerical oscillations. These oscillations arise from an error in computing the pressure on the faces between the two domains. The current numerical implementation of this interpolation selects an average interpolation of the pressure. But the pressure gradients are very different on both sides, because the friction terms are very different. The average face value does not account

for this, and this introduces oscillations in the pressure, which also affect velocities near these faces.

A numerical correction was derived [17] and is added to the momentum equation. We show in Figure 3 the effectiveness of this numerical correction at damping oscillations with various correction factors (f_{cf}). The theoretical value of the friction correction factor is 1.

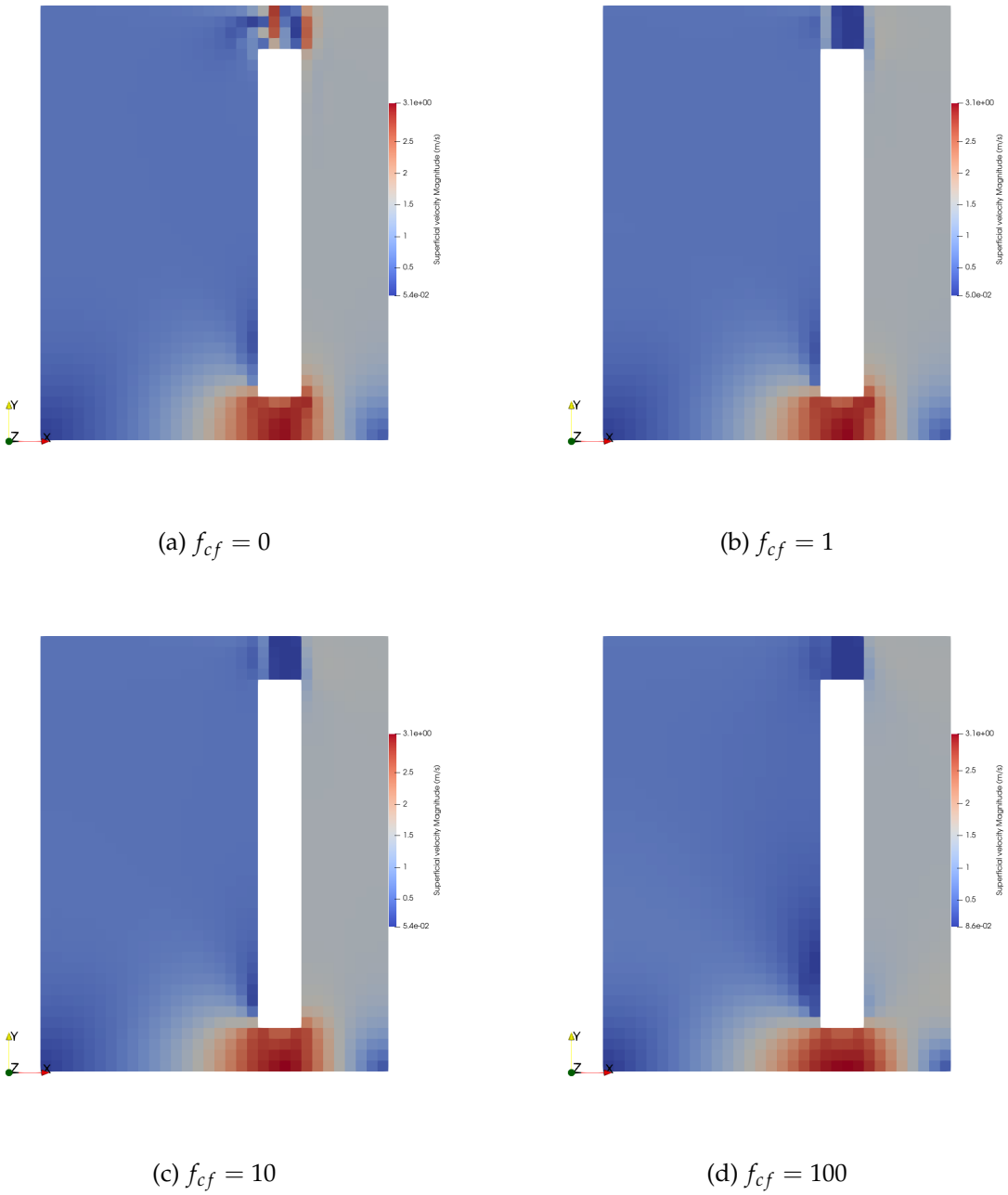

(a) $f_{cf} = 0$ (b) $f_{cf} = 1$

(c) $f_{cf} = 10$ (d) $f_{cf} = 100$

Figure 3: Velocity fields (coarse) at different friction correction factors.

3. MODEL DESCRIPTION

In Section 3.1, we introduce the Monte Carlo models used in this work to provide a measure of the highest fidelity solution possible with modern neutron transport methods. The Griffin equilibrium core model is described in Section 3.2. The thermal fluids model calculating the active core and structure temperatures is described in Section 3.3. In order to compute an accurate temperature feedback in a pebble-bed reactor, one must determine both the graphite (spectral hardening) and kernel (Doppler broadening) temperatures, which is discussed in Section 3.3.2. In Section 3.4, we describe how all of these MOOSE-based applications are coupled.

3.1 Serpent Equilibrium Core Model

We developed two Serpent models to benchmark the Griffin core solutions:

1. **Serpent-K**—based on the Kairos Power pass-averaged number densities for 88 isotopes in 40 fuel zones (four radial and 10 axial) that have been made publicly available [18]. This Serpent model uses equilibrium core FLiBe concentrations that are consistent with the Griffin model. This data set was generated from an equilibrium core reference solution with the Kairos Power Advanced Core Simulator (KPACS) model, which included 320 fuel zones (four radial and 10 axial and eight pebble passes) and the standard isotopes in Serpent [1].

2. **Serpent-G**—based on the Griffin equilibrium core number densities as described in Section 3.2 with equilibrium core FLiBe concentrations and 640 discrete zones (16 radial and 40 axial regions).

Both Serpent models use the same random distribution of pebbles and TRISO particles instead of using a lattice structure as was done for the MCNP-6.2 comparisons in [1]. The pebble and TRISO distributions were obtained with the particle distribution file generator in Serpent targetting the number of particles. The grow and shake algorithms were used with values of 0.1 for the shake factor and 0.05 for the particle growth rate. Although the pebble distribution solution from this packing algorithm is not physical, it provides an initial random distribution that is far superior to the lattice packing and captures the reduction in pebble packing near the

walls. Lattice packing is problematic because it creates characteristic neutron streaming paths. A coarse pebble packing fraction distribution is included in Table 8.

Table 8: Pebble packing fraction distribution (Computed by L.N. Carlson).

	Radial 1	Radial 2	Radial 3	Radial 4
Axial 1	0.604	0.599	0.600	0.594
Axial 2	0.600	0.600	0.599	0.599
Axial 3	0.598	0.601	0.600	0.597
Axial 4	0.601	0.599	0.600	0.597
Axial 5	0.599	0.600	0.600	0.601
Axial 6	0.600	0.600	0.600	0.599
Axial 7	0.600	0.600	0.600	0.599
Axial 8	0.599	0.600	0.599	0.600
Axial 9	0.599	0.599	0.598	0.599
Axial 10	0.598	0.600	0.601	0.592

The radial and axial view for the Serpent model are shown in Figure 1. The Serpent-K model with initial FLiBe concentrations yields an eigenvalue of 1.01401, which is consistent with Table 10 in [1]. The equilibrium core FLiBe concentrations used in all models is shown in Table 9.

Table 9: Equilibrium core FLiBe concentrations.

Isotope	Number density
Li-6	4.38333E-07
Li-7	2.40010E-02
F-19	4.80084E-02
Be-9	1.20001E-02

3.2 Griffin Equilibrium Core Model

The Griffin equilibrium core model consists of the cross sections described in the methods section and mesh files. Figure 4 depicts the transport solver mesh (a) and streamline mesh overlay (b) that identifies the location of the streamlines where the pebbles are depleted. The various cross-section regions are also identified in Figure 4(a) with the harder, interior spectral zone 1 and a softer, near reflector spectrum zone 2.

The standalone equilibrium model is used to compare to solutions from the KPATH [1] code. The Griffin calculations are performed with four energy groups to obtain an equilibrium configuration with 1% excess reactivity. To achieve this, we modify the burnup limit until the

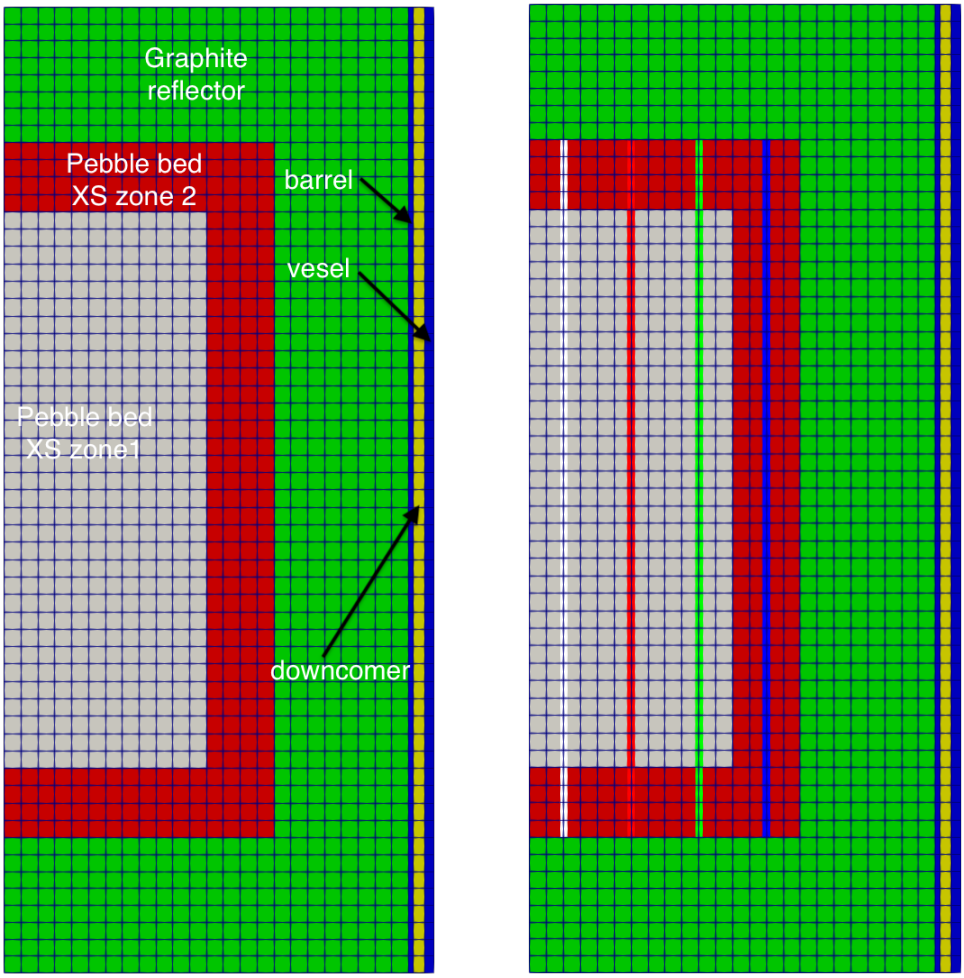

(a) Cross-section regions (b) Streamline overlay

Figure 4: Griffin equilibrium core mesh.

desired excess reactivity is obtained. The parameters used in the equilibrium core calculations are included in Table 10.

Table 10: gFHR model cross-section specifications.

Parameter	Value
Pebble types	One pebble type
Number of streamlines	4
Number of burnup groups	9
Approximate pebble residence time [days]	62.25
Pebble unloading rate [pebbles/min]	2.66

The neutronics model assumes that all of the temperatures in the core are 900 K except the fuel temperature, which is set to 959 K. With the equilibrium core, we then compute fuel, moderator, reflector, and salt void coefficients of reactivity as well as kinetic parameters. In a manner consistent with Reference [1], the temperate feedback of the cross sections is obtained via a 100 K perturbation, whereas the coolant density is perturbed by 2.5%.

3.3 Thermal Fluids Model

There is no detailed information on the thermal fluids design for the gFHR beyond what is provided in Reference [1]. Additional approximations were necessary to develop a model for transient analysis, including the unprotected loss of forced coolant (ULOF) event. Parts of the model described in Section 3.3.1 are based on simple schematics for the Hermes reactor [19], the rest have been assumed. The fuel and moderator temperatures necessary to couple the neutronics and thermal fluids are obtained from 1D pebble and TRISO conduction models described in Section 3.3.2.

3.3.1 Core Thermal Fluids Model

The Pronghorn core thermal fluids mesh is shown in Figure 5. A porous medium approximation is used in the flow regions shown in Figure 5(a), whereas a solid conduction model is used for the reflector, core barrel, and vessel, as shown in Figure 5(b).

The porous medium and solid models are currently only coupled via solid conduction heat transfer. Conjugate heat transfer is left for future work. The fluidic diode allows two possible flow

paths: force cooling (normal) operation and natural circulation. The two flow paths are shown in Figure 6.

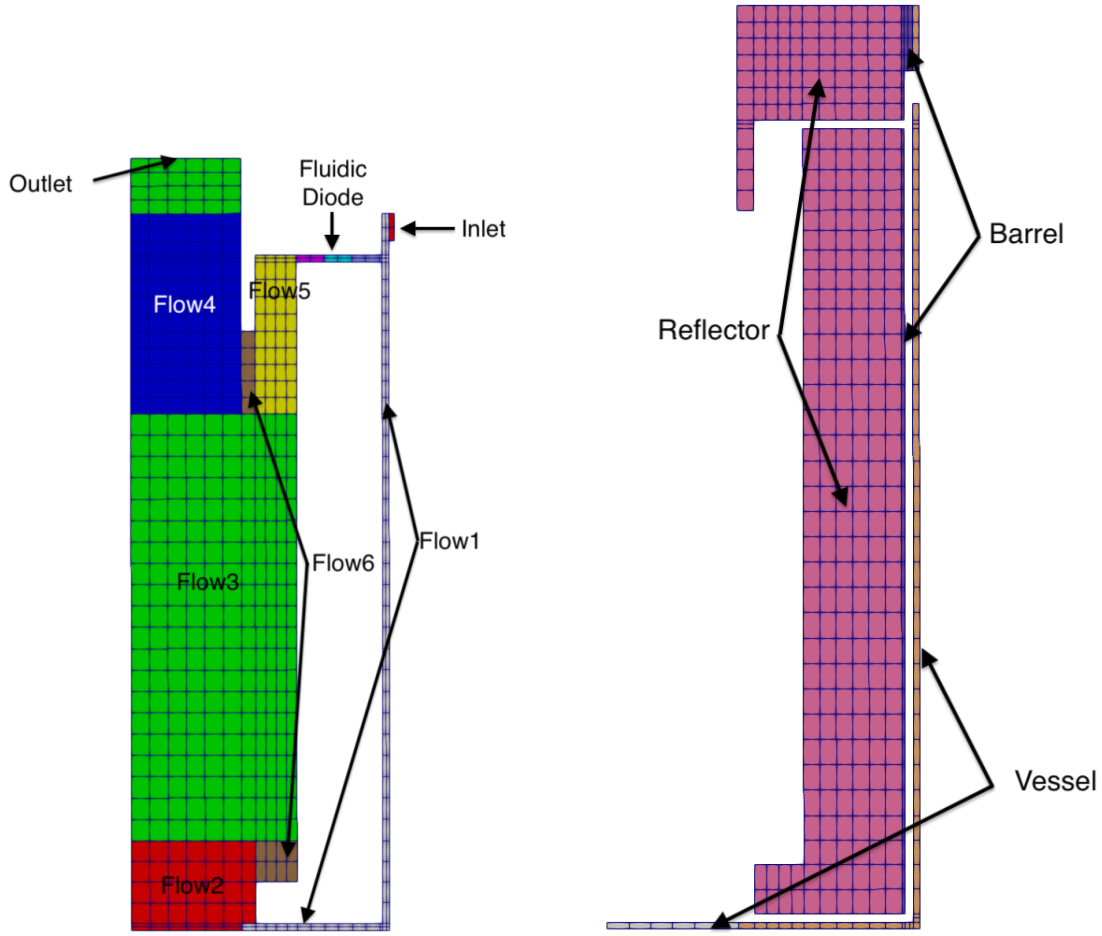

(a) Porous medium mesh (b) Solid conduction mesh

Figure 5: Pronghorn thermal fluids mesh.

The conceptual geometry of the gFHR model is shown in Figure 7. The region identification values shown in Figure 7 can be used as keys in Table 11 that summarize the parameters and closure correlations used in each region.

Areal heat transfer coefficients h computed using the Dittus-Boelter correlation are converted to volumetric heat transfer coefficients α by:

$$\alpha = \frac{A_{HT}}{V} h, \tag{15}$$

where A_{HT} is the heat transfer area of the region and V is the volume of the region. For the annular

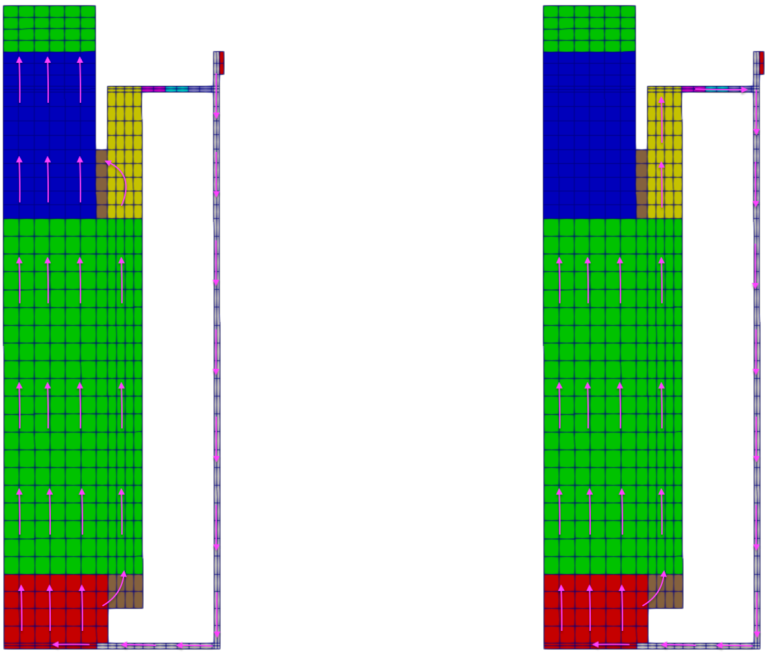

(a) Forced cooling (normal) (b) Natural circulation

Figure 6: Pronghorn flow path.

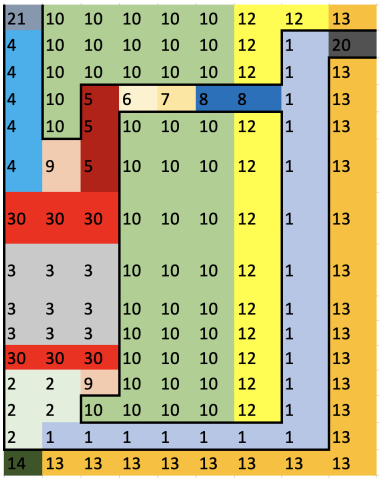

Figure 7: Region assignments for the Pronghorn gFHR model.

downcomer $\frac{A_{HT}}{V} = 4/(D_o - D_i) = 40\ \mathrm{m}^2/\mathrm{m}^3$.

The primary assumptions and limitations of this model are included in Section 3.5.

ID	Name	Porosity	D_H	κ_s	κ_f	Drag	α
1	Downcomer	0.999	0.1	k_s^*	k_f	Churchill	D-B
2	Cold plenum	0.9999	0.9	k_s^*	k_f	Open	0
3	Bed	0.401	0.04	PBR κ_s^a	Peclet dependent κ_f	KTA	Petrovic
4	Upper cone	0.75	0.04	PBR κ_s^a	Peclet dependent κ_f	KTA	Petrovic
5	Vertical duct to diode	0.9999	0.3	k_s^*	k_f	Open	0
6	Diode 1	0.9999	0.1	k_s^*	k_f	see description in text	D-B
76	Diode 1	0.9999	0.1	k_s^*	k_f	see description in text	D-B
86	Diode 1	0.9999	0.1	k_s^*	k_f	see description in text	D-B
4	Lower cone	0.75	0.04	PBR κ_s^a	Peclet dependent κ_f	KTA	Petrovic
10	Reflector	—	26	a	—	—	—
12	Barrel	0	—	21.5	—	—	—
13	RV 1	0	—	21.5	—	—	—
14	RV 2	0	—	21.5	—	—	—
20	Inlet	0.999	0.1	k_s^*	k_f	Churchill	0
21	Outlet	0.999	0.8	k_s^*	k_f	Open	0
30	Core buffer	0.999	1.2	k_s^*	k_f	Open	0

[a] Radiation: Breitbach-Barthels, Conduction: Chan-Tien, Fluid conduction: ZBS

Table 11: Modeling parameters and closure relations used in the Pronghorn gFHR model, where D_H is the characteristic length of each region, κ_s is the effective solid thermal conductivity, κ_f is the effective fluid thermal conductivity, α is the volumetric heat transfer coefficient. Regions with porosity equal to zero have no defined flow variable.

3.3.2 Pebble and Tristructural Isotropic Conduction Models

The pebble and TRISO particles are modeled with 1D steady-state solid conduction using Pronghorn. The thermal conductivity for the various materials is shown in Table 12. Note that the effective thermophysical properties for the TRISO and fueled regions of the pebble use the composite material theory described in the Pronghorn manual [16]. Currently, we only use a temperature dependence on the fuel kernel. Additional temperature, burnup, and fluence dependence will be added in future work as was done in Reference [10].

We impose Dirichlet boundary conditions on both the pebble and TRISO models and enforce the average homogeneous surface temperature from the porous medium solution on the pebble surface and pebble fuel region average temperature on the TRISO surface. In addition, we use a quasi-static assumption that although does not account for the thermal inertia of the pebble and the TRISO, it allows for simpler coupling and introduces a negligible error. More complex coupling approaches are left for future work. Typical solutions for the pebble and TRISO temperature fields are shown in Figure 8.

Table 12: Thermal conductivity of the various pebble and TRISO materials.

Material	Value [W/m/K]
Kernel	$\frac{1.0}{(0.035+2.25e-4*t)} + 8.30e-11*t^3$ []
Buffer	0.7
PyC	4.0
SiC	16.0
Matrix and shell	32.4
Core	30.0
TRISO effective	Composite solid properties series mixing
Pebble fuel region effective	Composite solid properties Chiew mixing

3.4 Equilibrium Core Coupled Model

The coupled model incorporates the significant phenomena that affect the neutronics feedback for the reactor. This includes all of the parameters identified in the cross-section preparation, see Section 2.1.1. BlueCRAB is the MOOSE-based wrapper-application that includes various dynamically linked applications. BlueCRAB enables the user to run various MOOSE-based

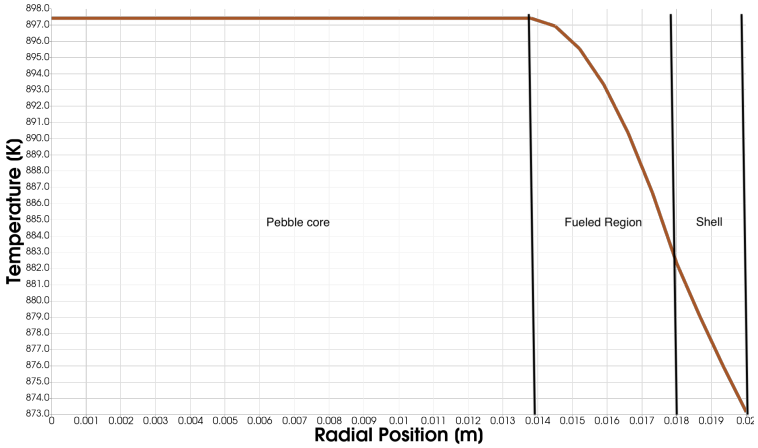

(a) Pebble temperature

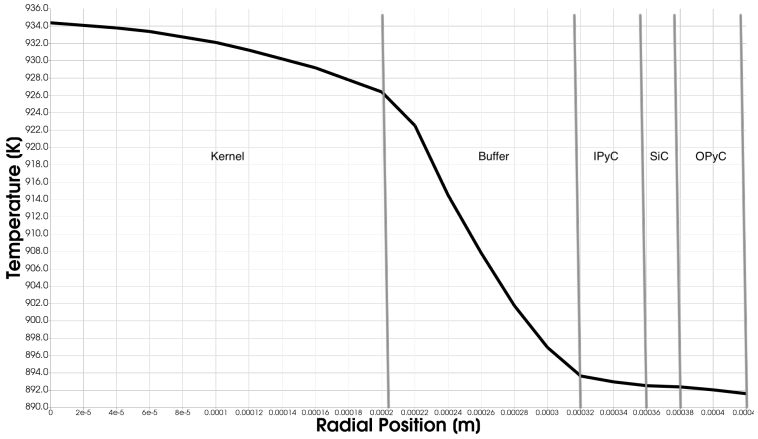

(b) TRISO temperature

Figure 8: Temperature profiles for the gFHR pebble and TRISO designs with an assumed power density of $5x10^7 W/m^3$.

application inputs via a single precompiled binary file on the INL HPC.

A schematic showing the NEAMS tools deployed in this analysis, and their interaction is shown in Figure 9. The main application input (MainApp) is the Griffin spatial flux and eigenvalue solution that creates MultiApps for Pronghorn (pseudo-transient thermal fluids), Griffin (streamline depletion), and Pronghorn (steady-state pebble and TRISO conduction). In this RZ model, Griffin creates one pebble and TRISO multiapp for each burnup group, and each MultiApp executes 640 SubApps (16×40 spatial grid) to obtain the graphite and fuel temperature field in the pebble-bed core. The variable transfers between the MainApp and MultiApps are shown in red arrows, whereas the varible transfers between the MultiApps and MainApp are shown in blue.

The order of execution is presented in Table 13. The calculation is initiated by the streamline-depletion solver, which initializes the number densities, then the pebble and TRISO thermal models update the moderator and fuel temperatures, followed by the flux and k-eigenvalue solve in the Griffin MainApp, and finally the full core thermal-fluids field updating with the latest power density. All the physics are converged in a Picard iteration at each time step before proceeding to the next time step.

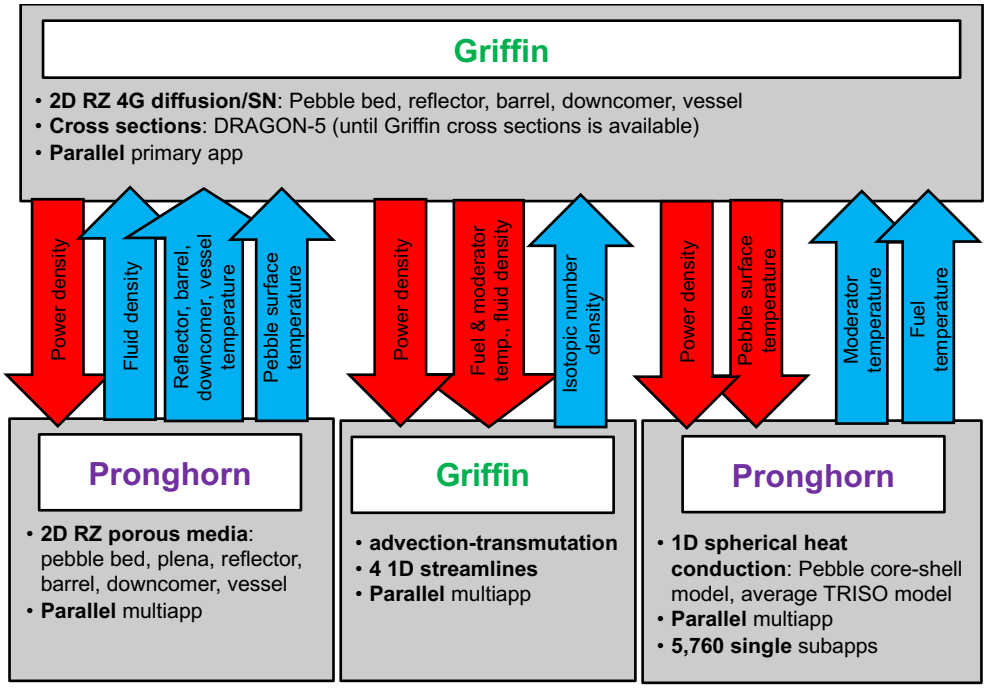

Figure 9: Multiphysics coupling for the asymptotic core calculation.

Table 13: Order of execution during the Picard iteration.

Application	Execution
Griffin flux and k-eigenvalue	between timestep_begin and timestep_end
Griffin streamline	initial and timestep_end
MOOSE Modules—pebble and TRISO thermal	timestep_begin
Pronghorn thermal fluids	timestep_end

3.5 Assumptions And Limitations

The following assumptions in the **neutronics model** are made:

1. A 2D RZ representation of the reactor core is used and is a good representation of the reactor geometry.

2. The multigroup neutron diffusion equation provides an accurate enough flux solution for the core and reflector regions for equilibrium core and time-dependent calculations.

3. The grey curtain used to model the control rods is not corrected using the superhomogenization (SPH) equivalence method since no reference solution is available for the equilibrium core calculations.

4. The multigroup cross sections are prepared using an infinite, reflected domain in the lattice physics calculation. The intracore neutron leakage significantly affects the local spectrum and will have an impact on the cross-section homogenization [10]. Nevertheless, cross-sections serve as an initial set to perform preliminary calculations until more sophisticated methods are available in Griffin.

5. A flux-limited approximation of the isotope transport cross sections is sufficient to build acceptable diffusion coefficients for this reactor.

6. A 1D streamline depletion is sufficient to capture the pebble flow since experiments show that the flow is axially dominated [20].

7. The equilibrium salt composition is approximated and not directly calculated in Griffin.

The assumptions and limitations applicable to the developed **thermal fluids model** are that:

1. Porous medium equations capture most of the important effects in the core.
2. The flow in the plena is approximated due to a lack of detailed information about the geometry and will require either empirical or CFD-computed closure models to be further improved but is not expected to significantly change the core temperature results.
3. Wall effects for convection, radiation, and conduction heat transfer are approximated not explicitly treated.
4. There is no convective heat transfer between the fluid and reflector regions, so we only considered conduction and radiation trough the pebbles.
5. Slip-wall and symmetry boundary conditions are used for the fluid mass, momentum, and energy equations.
6. All walls are adiabatic, and the conjugate heat transfer is treated as a volumetric phenomenon.
7. The solid energy equation boundaries are all adiabatic except for the outside of the vessel.
8. The volumetric friction diode requires a significant friction correction. A transition to a wall flow diode will remove this requirement in the future.
9. Radiative and convective boundary conditions were applied between the RV and RCCS.
10. The RCCS temperature is constant and set to 20^{o}C.
11. A solid temperature is defined everywhere even if the porosity is 1, which allows a reformulation of the areal heat transfer (as defined before) to volumetric heat transfer.
12. In regions where essentially no solid material is present, the solid thermal conductivity is set to $k_s^* = 10^{-4}$.
13. We use the molecular thermal conductivity of the fluid (k_f) instead of the effective fluid conductivity except for cases where we have a good model for the effective thermal conductivity (i.e., in the bed).

14. Heat transfer between the salt in the downcomer regions and the solid structure (reflector, barrel, and reactor vessel) is modeled as volumetric heat transfer.

15. Dittus-Boelter (DB) is used for modeling heat transfer between solid and fluid regions. We provide formulae on how to convert the areal heat transfer coefficient to a volumetric heat transfer coefficient.

16. In large open flow regions, we use a constant Forchheimer coefficient of 1.25. This corresponds to about 1 kPa of pressure drop per meter under forced flow conditions.

17. The diode region IDs 6–8 use Churchill drag coefficients and an additional Forchheimer coefficient of 100 and Darcy coefficient of 1,000 that are switched on during the steady state and switched off during the transient.

The following assumptions are applicable to the developed **pebble and TRISO thermal model**:

1. A thermal equilibrium approximation was considered in pebble simulations during transient calculations, thus using the quasistatic approximation in the pebble and TRISO thermal conduction problem is acceptable for slow transients since the two will be in thermal equilibrium and the Pronghorn solid conduction solution already includes the time-dependent term to compute the surface temperature.

2. Several sources of heat transfer heterogeneity around the pebble were ignored: the coolant flow orientation, pebble-to-pebble contact, pebble-to-reflector contact, and radiation.

3. A Dirichlet boundary condition is set at the pebble surface to obtain the moderator temperature and is assumed to provide reasonable solutions although it will not strictly conserve energy.

4. A Dirichlet boundary condition is set at the TRISO surface to obtain the fuel temperature and is assumed to provide reasonable solutions although it will not strictly conserve energy.

5. The thermophysical properties for the fuel kernel are based on UO_2 data, so ideally, we would need to use uranium oxycarbide data.

4. RESULTS

We first present the results of the Griffin equilibrium core calculation without thermal fluids feedback in Section 4.1. This model should be consistent with the Karios results in Reference [1]. We compare results with the Serpent models. This is followed by the coupled results in Section 4.2. Here we emphasize differences due to the temperature distributions. The results from the control rod withdrawal (CRW) transient are presented in Section 4.3 and the ULOF in Section 4.4.

4.1 Equilibrium Core Calculation

The fundamental mode eigenvalue (k_{eff}) and discharge burnup for the Griffin equilibrium core calculations are reported in Table 14. Recall that the discharge burnup in the Griffin models is modified to achieve an excess reactivity of 1% $\Delta k/k$ as was done with KPACS in Reference [1]. The results are obtained with the Griffin diffusion and SN transport solvers in four energy groups. We note that the discharge burnup predicted by Griffin is 10.7% (diffusion) and 7.4% (S12) lower than that reported value in Reference [1]. The discrepancy is even larger if one considers that the KPACS model appears to use initial FliBe compositions. These large differences can be attributed to a number of reasons, especially the microscopic cross sections in the Griffin model. We can directly identify differences with the "flux-limited" transport cross section used in the diffusion calculation since the predicted burnup is increased by 3.6% between diffusion and transport.

The k_{eff} from the 88 isotope model (Kairos-based number densities, Serpent-K) and 297 isotope model (Griffin-diffusion-based number densities, Serpent-G) are also included. In Reference [1], the author shows that the k_{eff} bias from the 88 isotope model is roughly +400 pcm. The reactivity bias in the Serpent-G model is thus -340 pcm. There are plans in the ART program to perform numerical benchmarks to verify the solution from the Griffin depletion calculations. In addition, these can be further improved with better cross-section preparation and by refining the broad group structure.

The radial and axial power profiles are included in Figures 10 and 11, respectively. The Griffin power profiles appear to be more consistent with the KPACS results included in Figures 14 and 12 in Reference [1] than with the Serpent model based on the 88 isotopes with 40 zones. This is observed in the axial profile 1.0 meter from the bottom of the active core where the KPACS

Table 14: Fundamental mode eigenvalues and discharge burnups for the equilibrium core. All models assume an equilibrium FLiBe concentration.

Model	k_{eff}	Discharge burnup $[J/m^3]$	Discharge burnup [EFPD]	Discharge burnup [MWd/kg]
Griffin EC Diff	1.01000	1.346E+15	466.0	153.3
Griffin EC S12	1.01000	1.387E+15	483.3	158.8
Serpent-K[1]	1.02905 $\pm$ 1.8 pcm	—	522[3]	—
Serpent-G[2]	1.02166 $\pm$ 3.2 pcm	—	—	—

[1] Based on KPACS number densities distributed by Karios Power
[2] Based on Griffin number densities computed from the equilibrium core diffusion solution
[3] Based on the KPACS reference solution with initial FliBe concentrations

prediction was above 2.5 W/m^3 but where the Serpent model predicts a peak value of 2.4 W/m^3. Griffin still underpredicts the peak power at the top of the active core. Note that discrepancies in the power density profile have been observed between Serpent MC and KP-AGREE solutions even when the cross sections were prepared with Serpent using the Kairos-provided equilibrium core number densities [21]. Currently, the Griffin solutions overpredict the axial and radial peaking away from the side and top reflector regions. We expect the Griffin solutions to further improve as the new cross-section preparation capability becomes available.

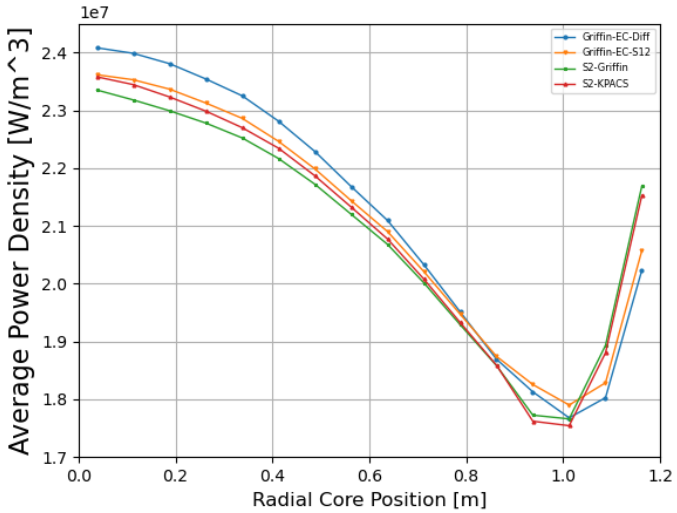

Figure 10: Griffin radial power shape of the equilibrium core gFHR.

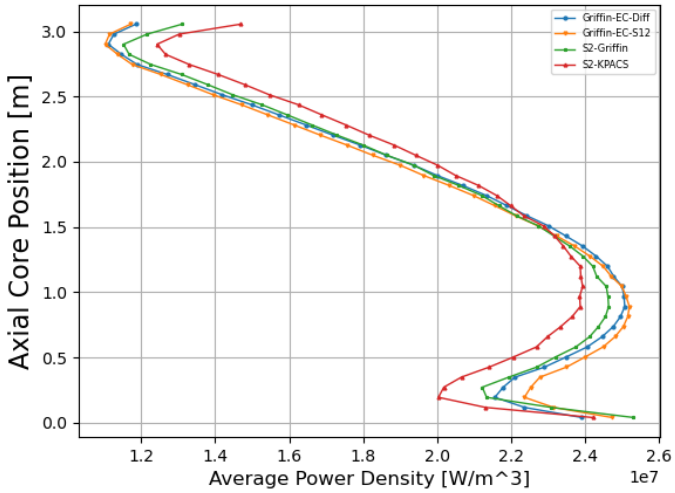

Figure 11: Griffin axial power shape of the equilibrium core gFHR.

The Serpent radial and axial profiles for the three different modeling approaches are shown in Figure 12. All the results from these models are consistent with the reported profiles in Figure 8 in Reference [1]. We note that the differences in the peaking near the axial reflectors in Figure 12(a) are probably due to finer tally bins used in the reference.

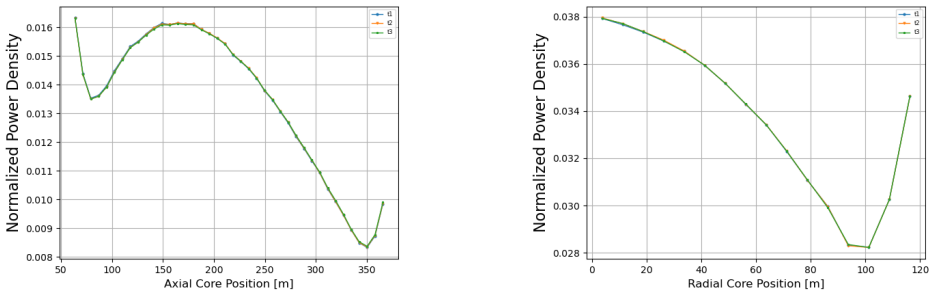

(a) Axial profile (b) Radial profile

Figure 12: Serpent power profile.

Comparisons of key isotopes between Griffin and KPACS equilibrium core solutions are shown in Table 15. There could be significant variability in these values due to the different discharge burnup limit for each solution, and further studies are warranted to better understand the differences, though these results are expected since it is well established that omitting the neutron leakage effects in the cross-section preparation primarily affects the higher actinide concentrations [10].

Table 15: Comparison of KPACS and Griffin isotopics.

Isotope	4G RMS ($\lvert e_{max} \rvert$)%
U_{235}	0.616 (1.378)
U_{238}	0.458 (1.107)
Pu_{239}	1.339 (2.689)
Pu_{240}	11.309 (17.491)
Pu_{241}	8.258 (12.997)
Xe_{135}	1.713 (4.227)

The coefficients of reactivity for the gFHR equilibrium core are shown in Table 16. Note that the current Griffin tabulation does not separate the coolant temperature and density, thus both components of the reactivity feedback are included in the Griffin result. Both the fuel and void coefficient of reactivity are consistent with the KPACS results, but the two coefficients that rely on graphite thermal scattering (moderator and reflector) do not. This could be attributed to differences in the S(α,β) thermal scattering treatment between the data sets, but further work is warranted to resolve this discrepancy.

Table 16: Coefficients of reactivity for the equilibrium core.

Reactivity coefficient	KPACS[1]	Griffin (4G)
Fuel temperature [pcm/K]	-4.56 $\pm$ 0.12	-4.59
Moderator temperature [pcm/K]	-0.4 $\pm$ 0.12	-0.84
Reflector temperature [pcm/K]	0.92 $\pm$ 0.12	0.37
Void [pcm/void%]	-48.19 $\pm$ 9.05	-59.34
Coolant temperature [pcm/K]	-1.2 $\pm$ 0.12	—

The kinetic parameters obtained with the IQS method in Griffin are included in Table 17. We also include the Serpent values obtained with the iterated fission probability method. Both the mean generation time (Λ) and effective delayed neutron fraction are consistent with the Serpent values.

Table 17: Kinetic parameters for the equilibrium core. Serpent values calculated with the iterated fission probability method.

			Griffin	Serpent		
Λ			3.75E-04	3.86E-04		
β_{eff}			5.36E-03	5.39E-03		
$\frac{\beta_{eff}}{\Lambda}$			14.29	13.96		
Precursor group	1	2	3	4	5	6
β Griffin	1.80E-04	1.01E-03	9.12E-04	2.01E-03	8.74E-04	3.48E-04
β Serpent	1.82E-04	1.02E-03	9.19E-04	2.03E-03	8.82E-04	3.54E-04
λ Griffin	1.33E-02	3.27E-02	1.21E-01	3.03E-01	8.49E-01	2.85E+00
λ Serpent	1.33E-02	3.22E-02	1.20E-01	3.02E-01	8.53E-01	2.86E+00

4.2 Coupled Equilibrium Core Calculation

Global results from the coupled steady-state calculation are included in Table 18. Here again the burnup limit is adjusted to produce a 1% $\Delta k/k$ reactivity bias, which slightly increases the discharge burnup for the coupled model. The coupled model includes nine burnup groups, each with distinctive fuel and moderator temperatures in each core mesh zone. The maximum fuel and moderator temperatures are approximately 5% higher than the core average with the current model where only the fuel includes temperature-dependent thermophysical properties. We expect this to increase in the future when we incorporate the temperature and fluence dependence of the various materials.

Table 18: Coupled equilibrium core results.

Parameter	Value
k_{eff}	1.01
Discharge burnup [EFPD]	468.2
Discharge burnup [MWd/kg]	153.8
FLiBe average density $[kg/m^3]$	1,982.5
T_{avg}^{fuel} [K]	953.6
T_{max}^{fuel} [K]	1004.7
T_{avg}^{mod} [K]	928.9
T_{max}^{mod} [K]	973.3
T_{avg}^{ref} [K]	858.9

We compare the axial and radial profiles of the uncoupled and coupled core in Figures 13. The differences in the profiles are consistent with the KPATH results reported in Reference [1] with the

largest difference in the lower core regions. In addition, we provide the core power distribution and the percent relative difference between the uncoupled and coupled models in Figure 14. As expected, the differences in the power solutions follow the gradient in the temperature field when compared to the core with a constant temperature.

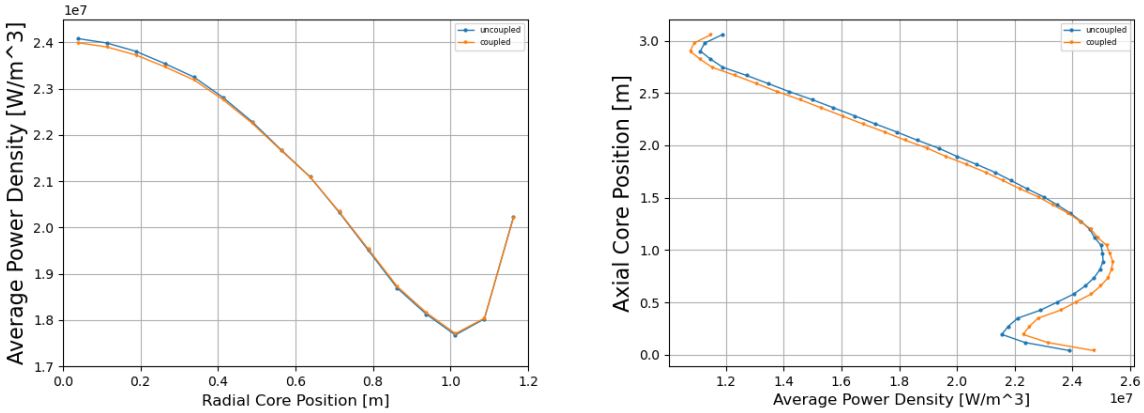

(a) Radial power (b) Axial power

Figure 13: Comparison of radial and axial powers between uncoupled and coupled calculations.

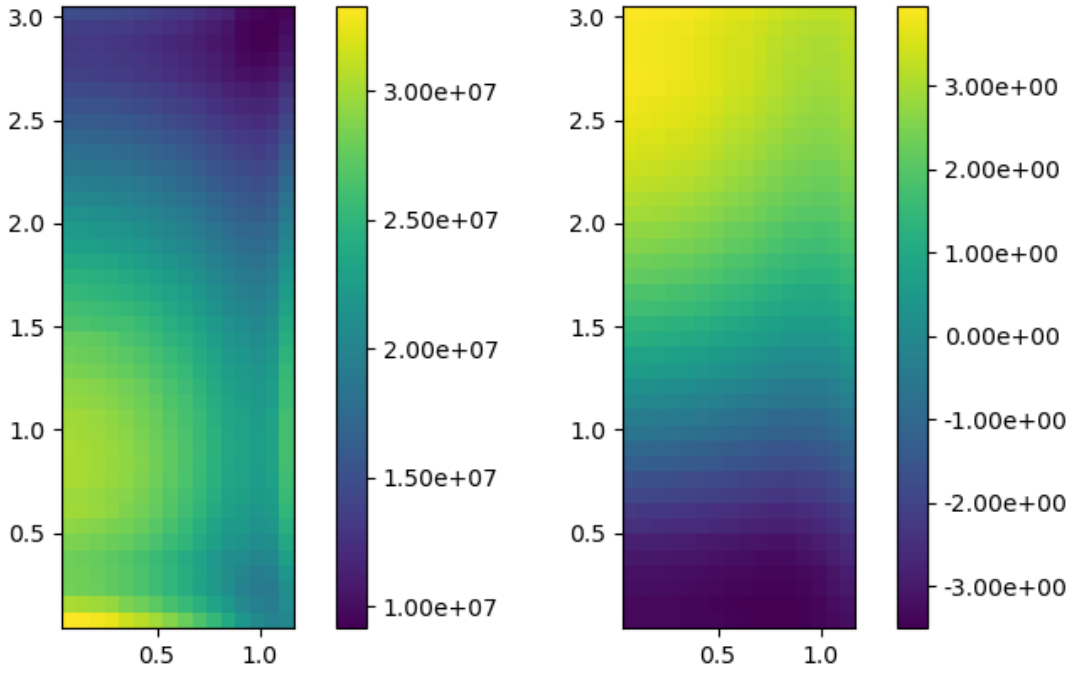

(a) Coupled power distribution [W/m^3] (b) Percent difference power distribution

Figure 14: Comparison of power distributions between uncoupled and coupled calculations.

The solid and fluid temperature fields are shown in Figure 15, and fluid density and pressure

in Figure 16. The peak temperatures are observed at the top of the active core region with a 300 K gradient across the height of the core. Temperature peaks in the solid materials appear near the reflector zones consistent with power peaks. The lower temperature in the reactor vessel and barrel reveal the enhanced heat transfer to and from the inlet coolant flow in the downcomer region. The current model of the fluidic diode exhibits a pressure gradient of 40 kPa with a temperature gradient of 80 K. The velocity field in Figure 17 shows an average velocity of 1 m/s in the downcomer region, except for the regions with sharp turns in which velocity increases due to the sudden changes in the flow direction. The flow area then expands when entering the core, thus reducing the velocity to 0.3 m/s. In the steady-state configuration for this model, no flow is allowed to pass through the fluidic diode, and it all exits at the core outlet.

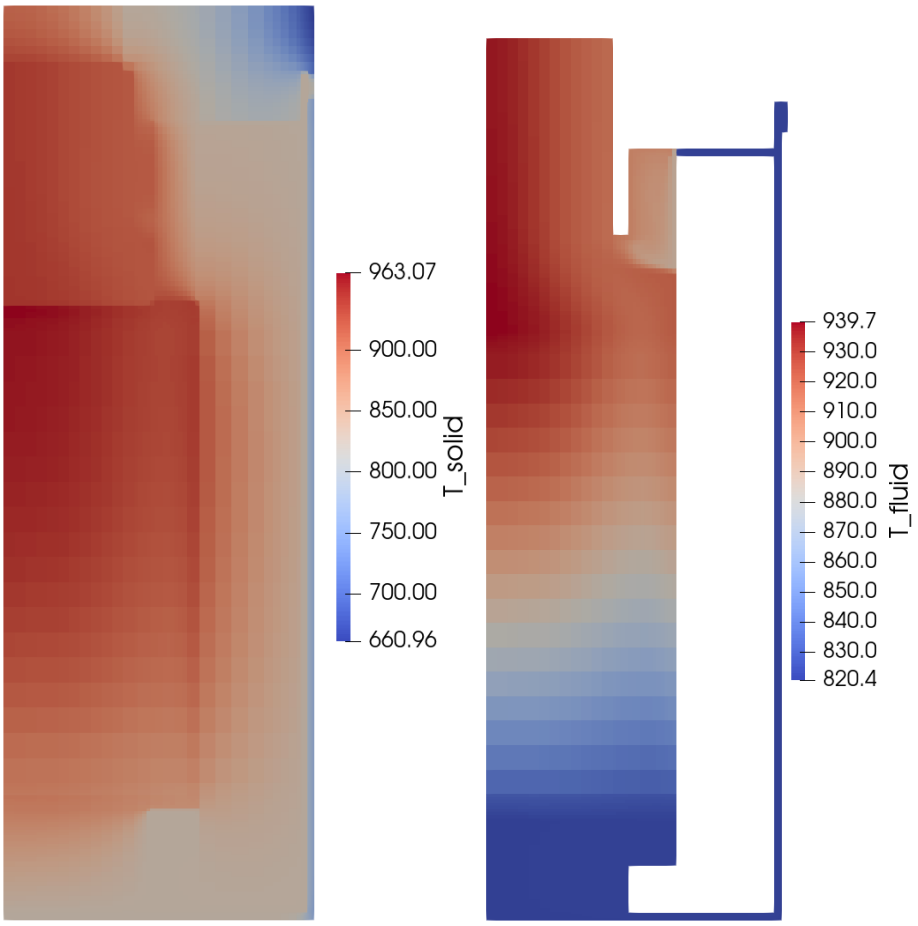

(a) Solid temperature [K] (b) Fluid temperature [K]

Figure 15: Steady-state core thermal solution.

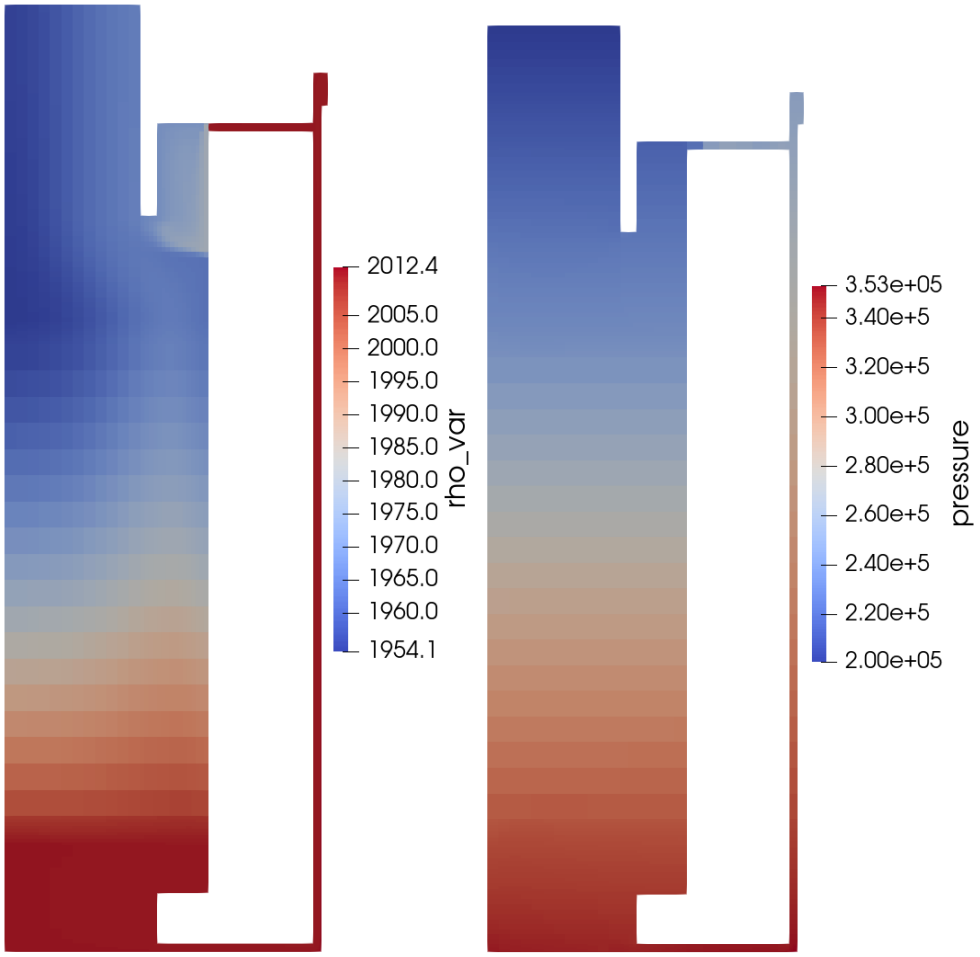

(a) Fluid density [kg/m^3] (b) Fluid pressure [Pa]

Figure 16: Steady-state core fluid density and pressure.

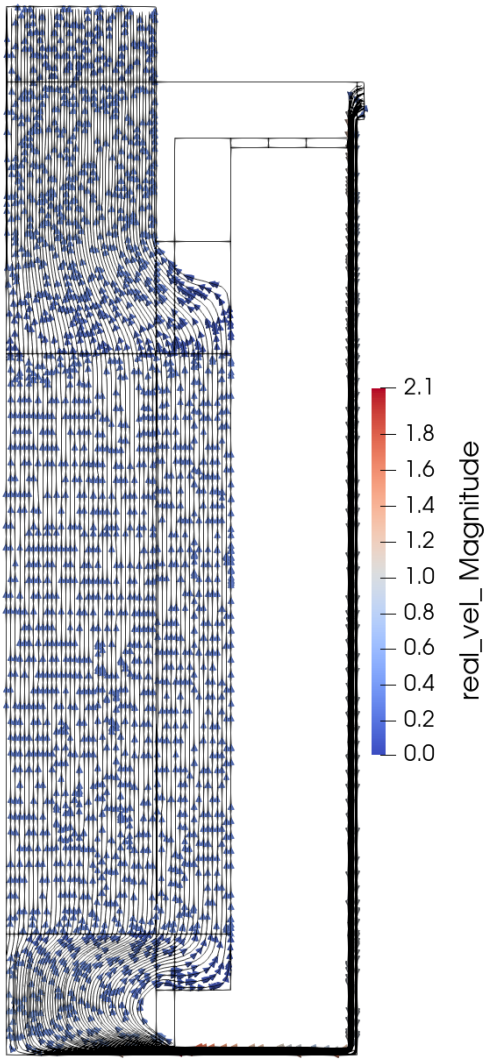

Figure 17: Steady-state fluid velocity [m/s].

4.3 Control Rod Withdrawl Transient

The gFHR core exhibits low excess reactivity like many online refueling pebble-bed reactor designs. The control rods are among the systems researchers can use to manage this excess reactivity. However, any malfunction of a control rod mechanism could lead to a CRW accident. In this section, a CRW transient scenario is simulated using a Griffin-Pronghorn sequence. A picture of the geometry is shown in Figure 18. This geometry is nearly identical to the gFHR geometry with the addition of the control rod. The control rod is 3.6947 cm long and uses B_4C as an absorbing material. We assume that FLiBe constitutes the unrodded fill material with any control rod movement.

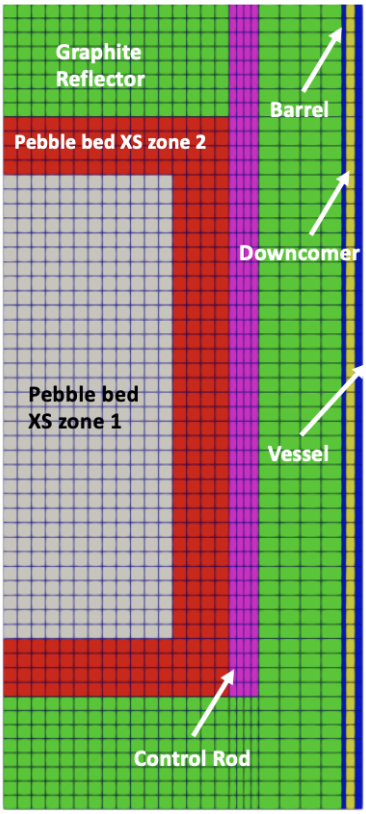

Figure 18: Griffin mesh with a control rod region.

To impose a suitable initial condition for the CRW transient, the control rod vertical position was adjusted to obtain a critical core configuration. The latter position was found using the automated criticality search executioner in Griffin [22]. The criticality search was performed in a multiphysics setting by including the thermal hydraulic feedback, computed with Pronghorn.

With this analysis framework, the critical control rod position was 2.614 m from the bottom.

Starting from the critical configuration from the criticality search, it is assumed a malfunctioning of the CRW mechanism leading to the transient scenario in which the accidental withdrawal of the control rod leads to the insertion of 345 pcm of reactivity (i.e., 65% of β_{eff}). The control rod position corresponding to 345 pcm of reactivity was found again using the criticality search executioner. Table 19 reports the control rod position at the beginning and end of each time interval $I_k = [t_k, t_{k+1})$. Linear interpolation is used to retrieve the value of the control rod position within each interval I_k. The control rod is removed at a rate of 1 cm/s.

Table 19: Control rod position at different times.

I_0	$t_0[s]$	$t_1[s]$	$f(t_0)[m]$	$f(t_1)[m]$
I_k	0	10	2.614	2.614
I_1	10	54	2.614	3.054
I_2	54	114	3.054	3.054
I_3	114	115	3.054	0.600
I_4	115	125	0.600	0.600

The prompt, decay, and total core power are shown as a function of time in Figure 19. Note that, in this simulation, the decay power remains constant until the SCRAM. The total power stabilizes to 413 $MWth$ when the control rod is at $3.054m$. This is due to the negative reactivity coefficient associated with the increase in fuel and moderator temperature and the expansion of the salt. The core physical quantities that drive these feedback mechanisms are shown in Figure 20. The curves obtained are smooth due to Griffin's de-cusping methodology. The results demonstrate the tight coupling between the pebble and salt temperatures that lead to the rapid changes in the salt density. The average and maximum temperature in fuel and moderator quickly stabilize when the control rod motion stops. In fact, all curves saturate to a maximum before rapidly decreasing once the control rod is inserted. The small dip in the power at 54 seconds is due to the delay in the temperature peak. The temperatures quickly reach thermal equilibrium after the SCRAM (recall the lack of decay heat energy in the pebble temperature model).

The opposite behavior is visible for the salt density, which decreases as the temperature increases before rapidly increasing during the control rod reinsertion in the interval I_3. A sequence of thermal flux shapes during the control rod movement are included in Figure 21. The

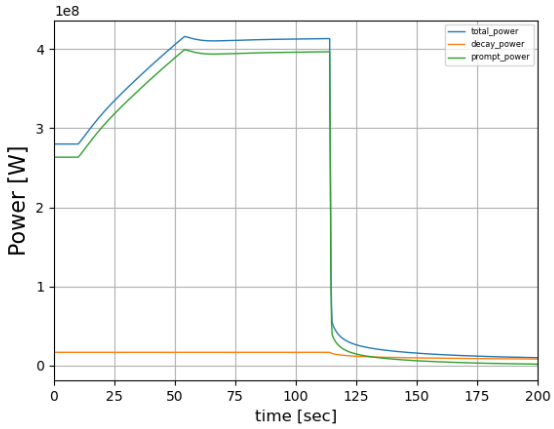

Figure 19: Reactor power during the CRW event.

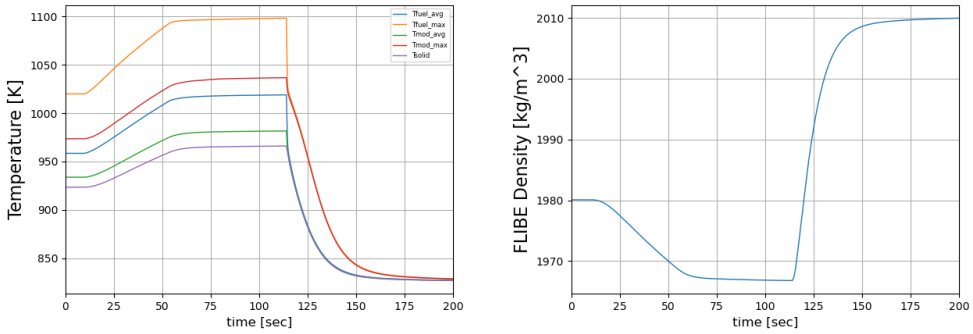

(a) Solid temperatures

(b) FLiBe salt density

Figure 20: Primary physical quantities that lead to negative feedback during the CRW event.

shape of the thermal flux peak present in the side reflector follows the rod withdrawal until the reactor SCRAM at 114 seconds. There is also a significant increase in the thermal flux magnitude in both the side and bottom reflectors following the control rod movement and, thus, the power ramp.

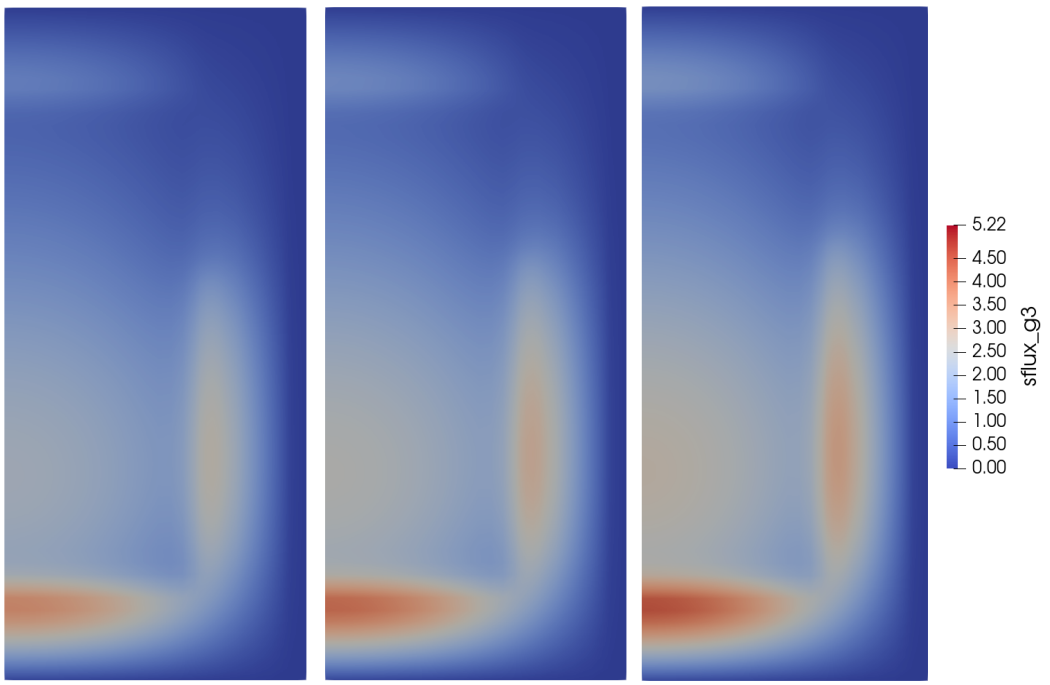

(a) 0 sec (b) 20 sec (c) 30 sec

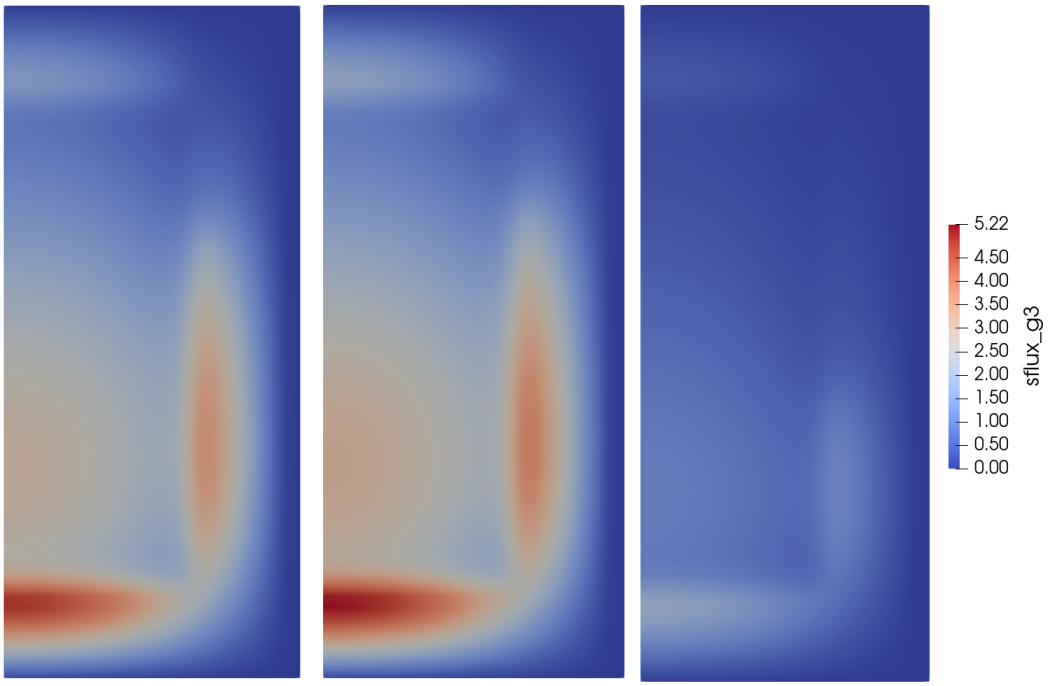

(d) 40 sec (e) 60 sec (f) 114.5 sec

Figure 21: Thermal flux shape during the CRW event.

4.4 Loss of Forced Flow Transient

The ULOF transient is generally one of the worst bounding accident cases that can affect this reactor design. The transient is defined by a complete loss of flow, whether through a ramp-down in pump power or a total blockage of one of the inlet pipes for the primary coolant system, and then it is unprotected in that no reactivity control mechanisms are actively controlled in shutting down the reactor. As a result of this transient, the reactor relies entirely on its internal reactivity feedback mechanisms to reach a new safe equilibrium or an approximate shutdown state. It is an approximate shutdown state because, without adding negative reactivity, it will settle on a new critical state that will potentially have a low power level, making it an approximate shutdown.

In the coupled problem, the loss of flow was modeled by changing the momentum inlet function instantaneously from the steady-state value to a no-flow condition. This is a bounding case with the complete inlet blockage to the reactor core. It is possible to model this with a mass flow rate ramp-down to simulate a pump loss of power or shutdown, if needed.

For this transient, it is important to understand the power and temperature behavior over time. We expect that, with the loss of coolant flow, the solid temperature will rise as energy accumulates in the solid core region. With this rise in temperature, there will be a subsequent drop in power as a result of negative temperature feedback from the fuel and moderator temperatures. In addition, there will be a slightly delayed negative feedback from the salt expansion due to the good heat transfer characteristics between the pebble and salt. The system is designed to create a natural circulation flow path through the fluidic diode that will move heat from the active core to the reflector graphite and steel structures and finally to the RCCS. This behavior is observed in the simulation results presented in the following figures.

The total, prompt, and decay power is shown in Figure 22. The prompt fission power decreases by an order of magnitude in the first 100 seconds and then proceeds to be further reduced by three orders of magnitude in the first 6 hours. The decay power, which at the steady-state equilibrium level is 15.75 MW (6.3%), decreases to 2 MW after six hours. The power level is in a stabilizing trajectory to a new steady-state condition since we can observe the fission power increasing again due to the change in the balance of the reactivity feedback, but that could also be due to numerical convergence of the fission source.

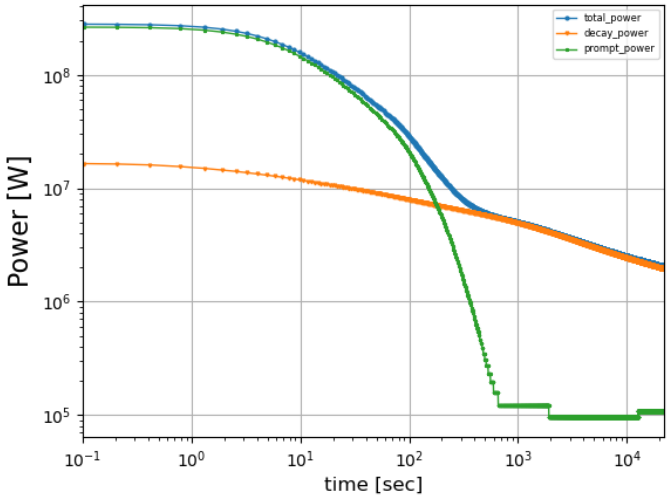

Figure 22: Power as a function of time during the ULOF event.

The primary physical quantities that lead to feedback effects are presented in Figure 23. In Figure 23(a), the fuel and moderator temperatures quickly climb at the beginning of the transient. The fuel and graphite moderator temperatures reach a thermal equilibrium due to the lack of the decay power in the pebble and TRISO model. The solid temperature then decreases as the heat moves directly into the reflector via pebble conduction and into the coolant via convection. A time sequence of the solid temperature field is included in Figure 25 and clearly shows the initial heat up and heat dissipation throughout the outer structures as time elapses. The coolant temperatures at various positions are presented in Figure 23(b) with the highest temperature in the core and upper flow regions near the outlet. The plot also shows how the FliBe temperatures are starting to move toward thermal equilibrium. A time sequence of the fluid temperature field is included in Figure 26 that shows the progression from the steady state to 6 hours into the transient. We observe the initial heat up of the coolant and its subsequent cooling as energy is deposited into the graphite and steel structures. The FLiBe density as a function of time is shown in Figure 23(c). Note that the decrease in the Flibe density beyond the steady-state point implies negative feedback, while the opposite leads to positive reactivity. The reactivity becomes positive again 3 hours into the transient from the imbalance between the feedback reactivity from the fuel and moderator temperatures, fluid density, and reflector temperature. The increase in the reflector temperature does increase the reflection of neutrons back into the active core region and thus

injects positive reactivity.

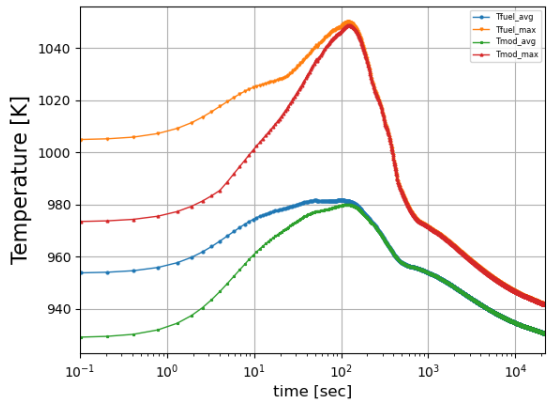

(a) Fuel and moderator temperatures

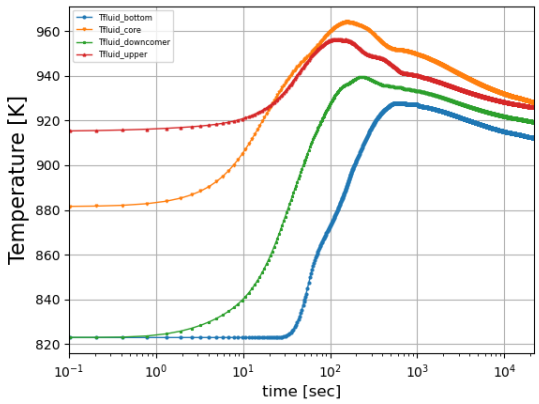

(b) Fluid temperature

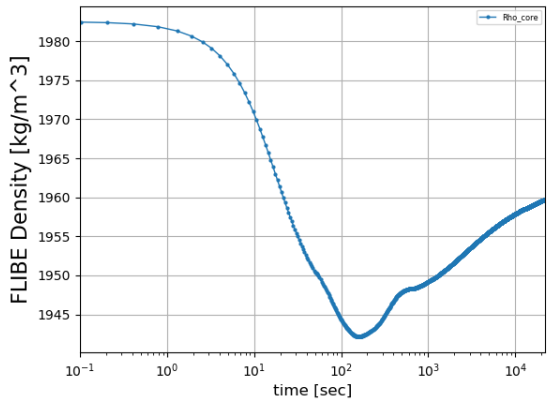

(c) FLiBe density

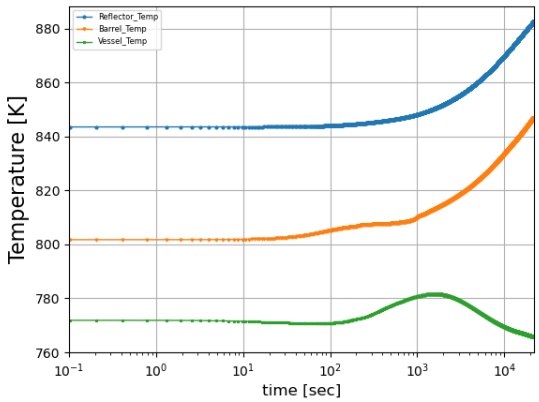

(d) Structure temperature

Figure 23: Primary physical quantities that lead to negative feedback during the ULOF event.

Recall that, during this transient event, the energy moves into structures, as seen in Figure 23(d). We see the changes in temperature in the reflector, barrel, and vessel. For the vessel temperature, we can observe an initial cooling effect from the RCCS. The vessel later heats up as the salt moves heat to this region, and finally the RCCS is able to remove heat more efficiently through the boundary. The heat flux at the boundary of the reactor vessel in Figure 24 relates the effects from the salt temperature in the downcomer region.

The onset of natural circulation is an important design feature of this reactor, and the time sequence of the velocity is presented in Figure 27. Once the inlet flow is blocked, there is a sudden change in the pressure across the fluidic diode that rapidly forces the flow from the core region into the downcomer, thus initiating the natural circulation flow. Note that, in the current model,

there is still a mass and energy exchange with the normal outlet, which can improve as more design details become available.

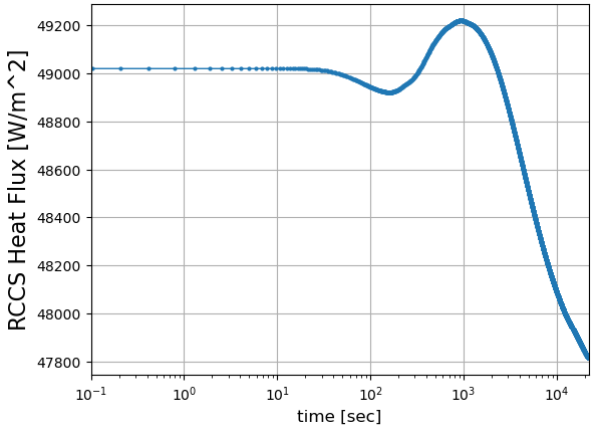

Figure 24: Heat flux to the RCCS.

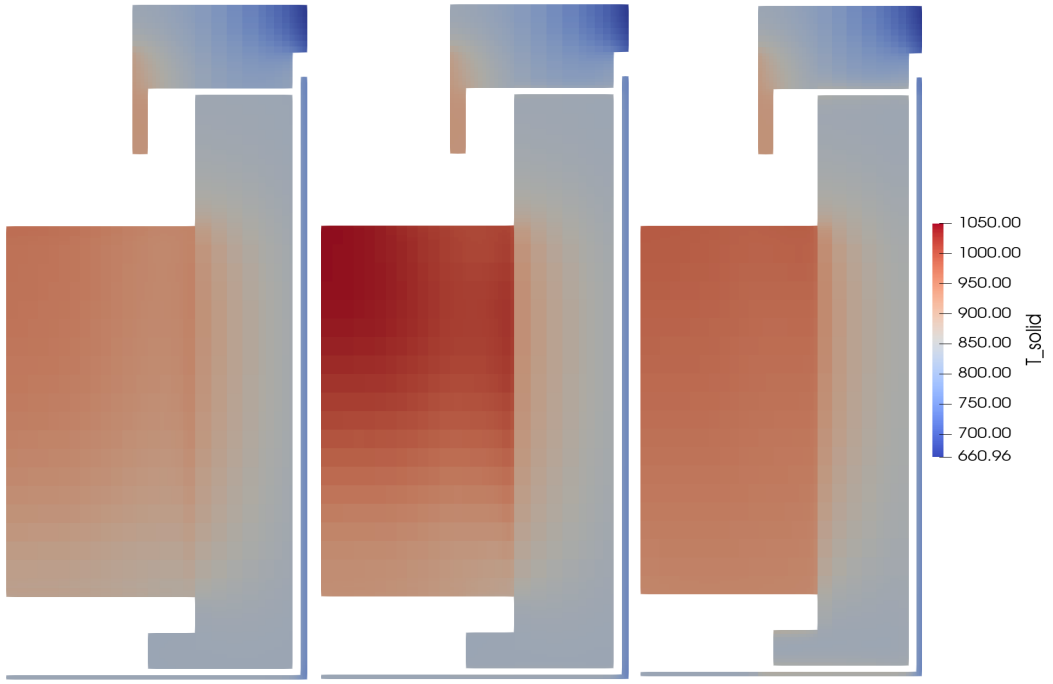

(a) 0 sec (b) 100 sec (c) 500 sec

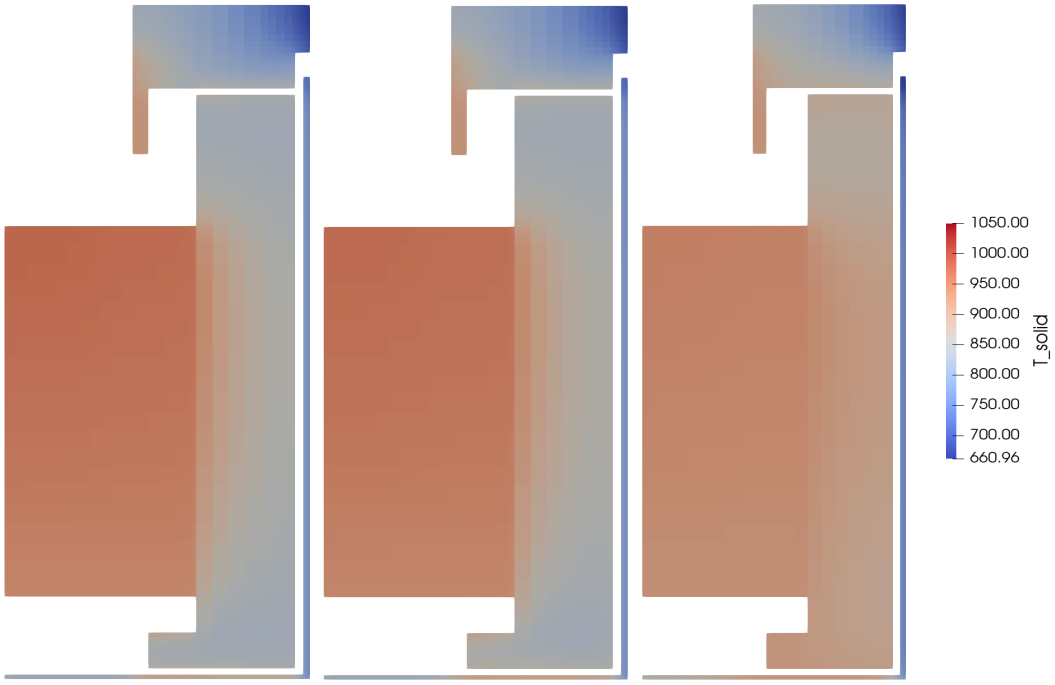

(d) 1,000 sec (e) 1,502 sec (f) 6 hrs

Figure 25: ULOF solid temperatures.

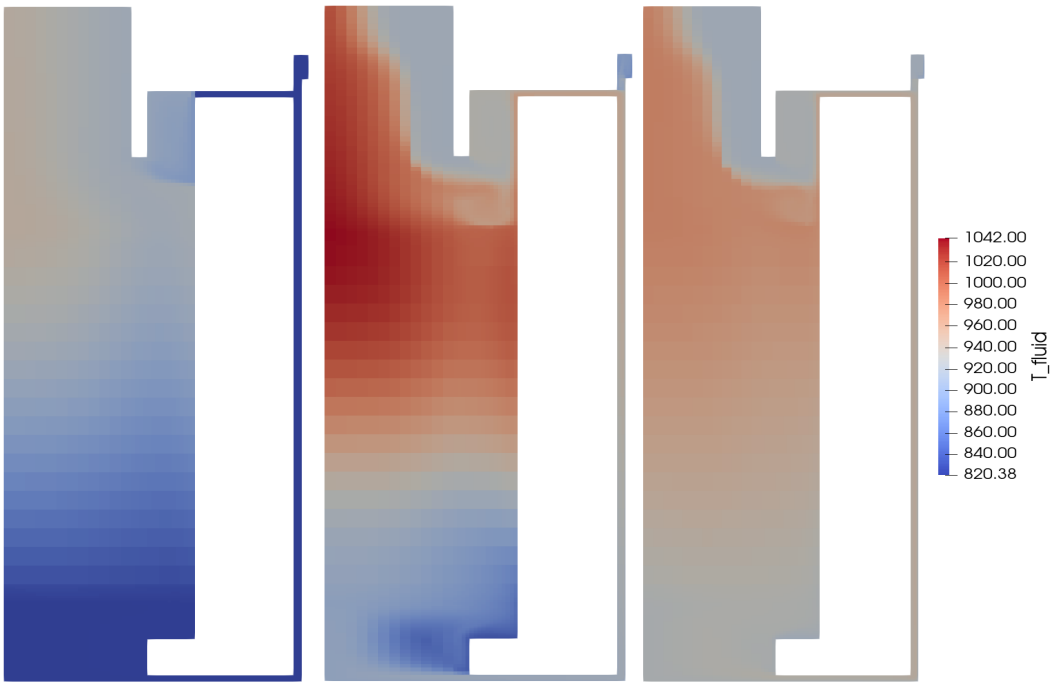

(a) 0 sec (b) 100 sec (c) 500 sec

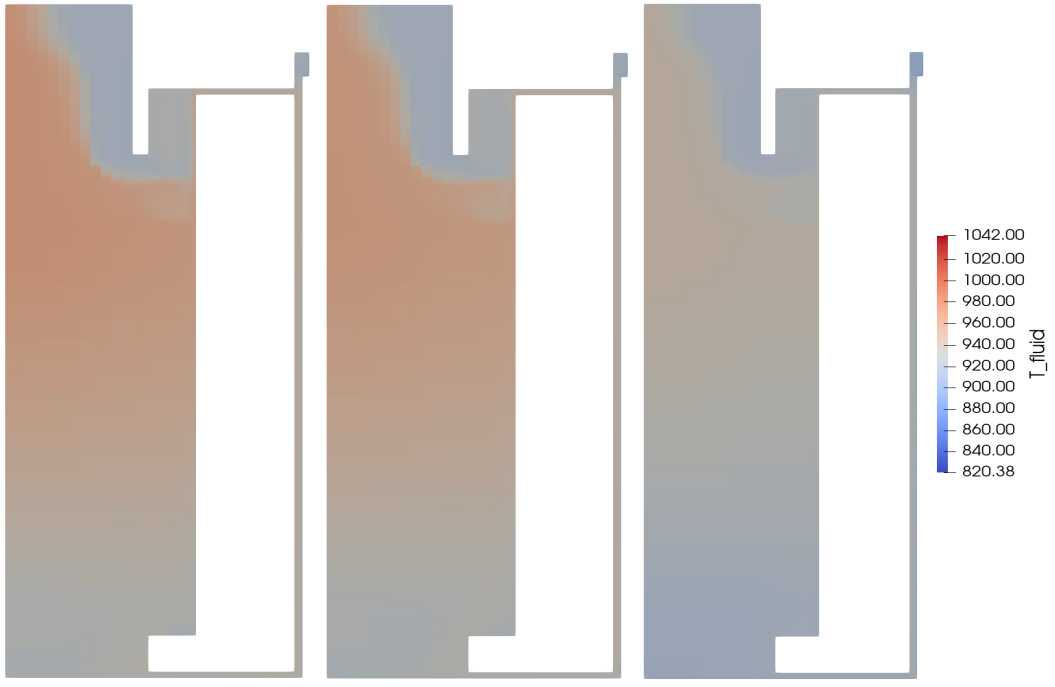

(d) 1,000 sec (e) 1,502 sec (f) 6 hrs

Figure 26: ULOF fluid temperatures.

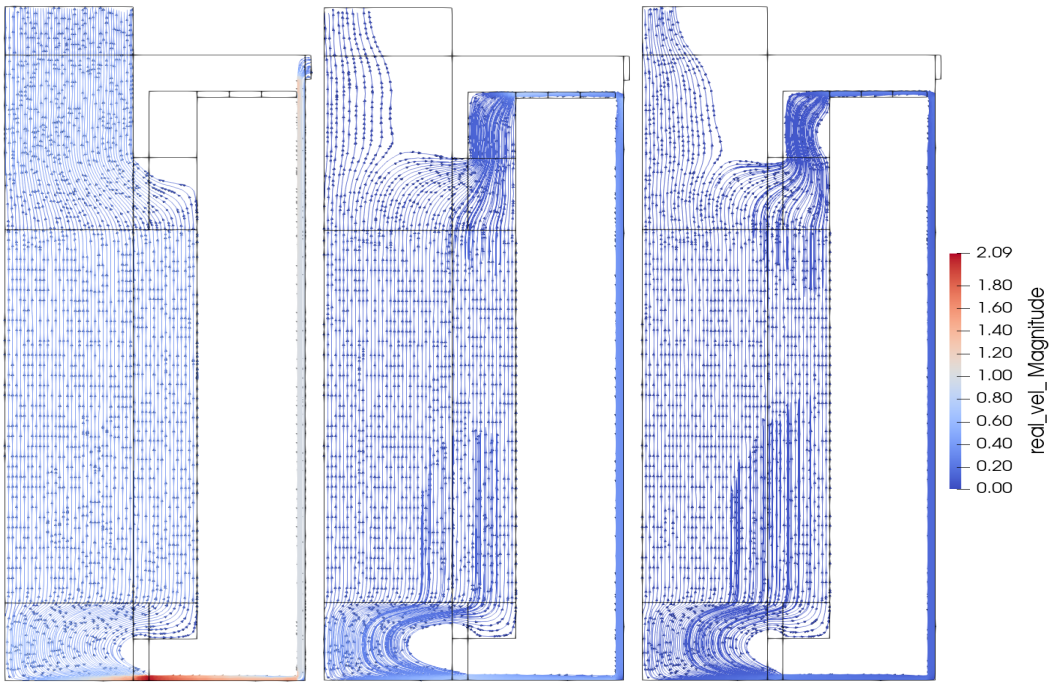

(a) 0 sec (b) 0.78 sec (c) 6.8 sec

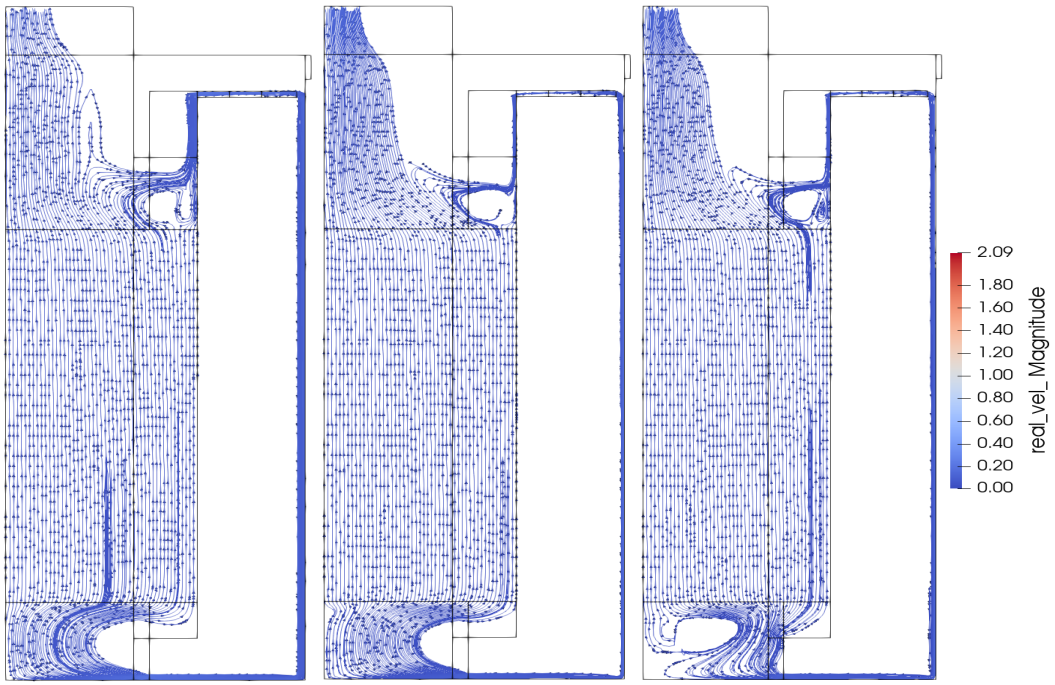

(d) 50 sec (e) 500 sec (f) 1,502 sec

Figure 27: ULOF fluid velocity.

5. CONCLUSIONS

Here we demonstrate the modeling and simulation of a gPBR with BlueCRAB.

We present Griffin results with four neutron energy groups based on diffusion and SN transport for the standalone (uncoupled) equilibrium core calculation in order to assess the difference between the approximations to the linearized Boltzmann transport equation. We develop two Monte Carlo Serpent models based on equilibrium number densities from Kairos' KPACS and Griffin. The SN power distributions compare well with Monte Carlo Serpent models, whereas the flux-limited diffusion coefficients appear to degrade the quality of the diffusion solutions. Although, significant approximations are made in the preparation of microscopic cross sections, the simulation results are consistent with published work by Kairos Power and other research entities. The fuel and salt void coefficients are in-line with the published works, but there are discrepancies in the graphite coeficients of reactivity that arise due to differences in the thermal scattering treatment in the cross sections. The point kinteic parameters are also consistent with the Monte Carlo results. The fully coupled Griffin neutronics and Pronghorn thermal hydraulics model is used to produced a steady-state solution of the equilibrium core and initial condition for various transients. The steady-state results are consistent with published work by Kairos Power. We exclusively deploy diffusion for all time-dependent solutions as a matter of practicality in these initial results.

Two transient scenarios are explored: ULOF and CRW. For the ULOF, we demonstrate using the Pronghorn fluidic diode model to simulate the transition from forced to natural convection for this reactor design. Although no design details are available, the simplified design presented here does successfully lead to the onset of natural circulation. We observe that the reactor effectively moves heat from the core region into the structures and ultimately the RCCS. Over time, and without any active reactivity control, the reactor starts to achieve a new, very low power level. The accidental CRW presented involves the insertion of 345 pcm (65 cents) of reactivity over 44 seconds. The reactor quickly self-stabilizes to a new, higher power level until the control rods are fully reinserted.

This coupled model is an initial prototype of the reference plant model and will be improved in future work.

6. FUTURE WORK

Future work for the neutronics model includes:

- Adopting the Griffin on-line cross section preparation workflow
- Deploying SN transport for transient simulations
- Improving the control rod modeling
- Developing a 3D model of the core to better assess the effect from control rod positioning
- Investigating different energy group structures
- Adding cone regions to the model
- Deploying Griffin's time-dependent depletion algorithm for the burn-in phase to assess intermediate cores between the initial start-up and equilibrium core
- Updating the model to the latest Griffin syntax
- Adding the Griffin PBR decay heat model

Future work for the Pronghorn thermal fluids model includes:

- Adding variable porosity
- Improving loss coefficient correlations in various regions
- Improving effective conductivity model for salt coolants instead of using ZBS model
- Implementing a sideset-based diode in the bypass channel instead of a volumetric term, which will facilitate cutting the flow in one direction without resorting to a locally large friction coefficient, which may be affecting the numerical system convergence
- Adding more detailed information about the plena geometry and use either empirical or CFD-computed closure models
- Improving RCCS modeling

Future work for the pebble and TRISO thermal models includes:

- Considering burnup and fluence dependence of the thermophysical properties
- Adding a decay heat source in the pebble and TRISO models (this is a new feature in Griffin and has yet to be incorporated to this model)
- Deploying fuel performance modeling in key regions as a post processing step for transients
- Robin boundary condition that couples directly to the fluid temperature via the heat transfer coefficient to improve energy conservation
- A Neumann boundary condition imposed on the TRISO surface to improve energy conservation
- Add a time dependent kernel with the heat capacity and density to conserve thermal inertia

REFERENCES

[1] N. Satvat, F. Sarikurt, K. Johnson, I. Kolaja, M. Fratoni, B. Haugh, and E. Blandford, "Neutronics, thermal-hydraulics, and multi-physics benchmark models for a generic pebble-bed fluoride-salt-cooled high temperature reactor (fhr)," *Nuclear Engineering and Design*, vol. 384, p. 111461, 2021.

[2] EPRI, "Uranium Oxycarbide (UCO) Tristructural Isotropic (TRISO) Coated Particle Fuel Performance: Topical Report EPRI-AR-1(NP)," Research Report 3002019978, Electric Power Research Institute, 2020.

[3] D. R. Gaston, C. J. Permann, J. W. Peterson, A. E. Slaughter, D. Andrs, Y. Wang, M. P. Short, D. M. Perez, M. R. Tonks, J. Ortensi, L. Zou, and R. C. Martineau, "Physics-based multiscale coupling for full core nuclear reactor simulation," *Annals of Nuclear Energy*, vol. 84, pp. 45–54, 2015.

[4] Y. Wang, S. Schunert, J. Ortensi, V. Laboure, M. DeHart, Z. Prince, F. Kong, J. Harter, P. Balestra, and F. Gleicher, "Rattlesnake: A moose-based multiphysics multischeme radiation transport application," *Nuclear Technology*, vol. 207, no. 7, pp. 1047–1072, 2021.

[5] F. N. Gleicher and J. Ortensi et. al., "The coupling of the neutron transport application RATTLESNAKE to the fuels performance application BISON," in *International Conference on Reactor Physics (PHYSOR 2014)*, (Kyoto, Japan), May 2014.

[6] Y. S. Jung and C. H. Lee, "PROTEUS-MOC User Manual," Technical Report ANL/NE-18/10, Argonne National Laboratory, September 2018.

[7] G. Marleau, A. Hebert, and R. Roy, "A user guide for dragon version5," Tech. Rep. IGE–335, Ecole Polytechnique de Montreal, 10 2020.

[8] R. Chambon, "HTR10 Modeling with DRAGON & DONJON," tech. rep., Ecole Polytechnique of Montreal, 2019.

[9] J. Leppänen,, *Development of a New Monte Carlo Reactor Physics Code*. PhD thesis, Helsinki University of Technology, 2007.

[10] J. Ortensi and P. Balestra, "Initial study on cross-section generation requirements for a PBR equilibrium core," PHYSOR 2022, Making Virtual a Reality - Advancements in Reactor Physics To Leap Forward Reactor Operation and Deployment, 2022.

[11] Z. L. et al., "Cumulative migration method for computing rigorous diffusion coefficients and transport cross sections from Monte Carlo," *Annals of Nuclear Energy*, vol. 112, p. 507–516, 2018.

[12] A. YAMAMOTO, Y. KITAMURA, and Y. YAMANE, "Simplified treatments of anisotropic scattering in lwr core calculations," *Journal of Nuclear Science and Technology*, vol. 45, no. 3, pp. 217–229, 2008.

[13] Y. Wang, S. Schunert, J. Ortensi, V. Laboure, M. DeHart, Z. Prince, J. Harter, J. Hanophy, O. Calvin, C. Lee, Y. Jung, H. Park, and S. Kumar, "Griffin Reactor Multiphysics Application Manual." `https://griffin-docs.hpc.inl.gov/latest/index.html`, 2022.

[14] G. L. Giudicelli, A. D. Lindsay, R. Freile, and J. Lee, "NEAMS-TH-CRAB," Tech. Rep. INL/EXT-21-62895, Idaho National Laboratory, 2021.

[15] G. Giudicelli, A. Lindsay, P. Balestra, R. Carlsen, J. Ortensi, D. Gaston, M. DeHart, A. Abou-Jaoude, and A. J. Novak, "Coupled multiphysics transient simulations of the mk1-fhr reactor using the finite volume capabilities of the moose framework," in *Mathematics and Computation for Nuclear Science and Engineering*, American Nuclear Society, 2021.

[16] A. Novak, S. Schunert, R. Carlsen, P. Balestra, D. Andrs, J. Kelly, R. Slaybaugh, and M. R., "Pronghorn theory manual," Tech. Rep. INL/EXT-18-44453-Rev001, Idaho National Laboratory, 2020.

[17] "Friction correction kernel documentation." `https://mooseframework.inl.gov/source/fvkernels/PINSFVMomentumFrictionCorrection.html`. Accessed: 2022-06-15.

[18] Kairos Power LLC., "Equilibrium Core Concentrations." `https://kairospower.com/generic-fhr-core-model`, 2021.

[19] Kairos Power LLC., "Hermes Non-Power Reactor Preliminary Safety Analysis Report - Non-proprietary," Tech. Rep. HER-PSAR-001, rev 0, Kairos Power LLC., September 2021.

[20] A. C. Kadak and M. Z. Bazant, "Pebble flow experiments for pebble bed reactors," 2004.

[21] E. M. Duchnowski and N. R. Brown, "Multi-physics modeling of fluoride-salt-cooled high-temperature reactor," in *2022 ANS Annual Meeting, June 12-16, Anaheim, CA*, 2022.

[22] J. Ortensi, Y. Wang, V. M. Laboure, Z. M. Prince, C. Lee, Y. S. Jung, H. Park, and E. R. Shemon, "Griffin software development plan," tech. rep., Idaho National Laboratoy, 2021.